Process Optimization of Alloyed Aluminum Backside Contacts for Silicon Solar Cells

Lynn Louise Chalfoun

B.S., Rutgers College of Engineering, 1990
B.A., Douglass College, 1990

Submitted to the Department of Materials Science and Engineering
at the Massachusetts Institute of Technology in partial fulfillment
of the requirements of the degree

Master of Science
in Materials Science

June 1996

Author.....
Department of Materials Science and Engineering
May 10, 1996

Approved by.....
Lionel C. Kimerling
Thomas Lord Professor of Materials Science and Engineering
Thesis Supervisor

Certified by.....
Michael F. Rubner
TDK Professor of Materials Science and Engineering
Chair, Departmental Committee on Graduate Students

Process Optimization of Alloyed Aluminum Backside Contacts for Silicon Solar Cells

by

Lynn Louise Chalfoun

Submitted to the Department of Materials Science and Engineering
at the Massachusetts Institute of Technology on May 10, 1996 in partial fulfillment
of the requirements of the degree Master of Science in Materials Science

Alloyed aluminum backside contacts are known to improve silicon solar cell performance. This enhancement is accomplished by gettering and by the repulsion of minority carriers from the rear contact of the cell by a highly doped p+ layer causing a reduction in effective surface recombination velocity. By examining how the p+ layer is influenced by processing and by modeling gettering mechanisms, we are able to suggest ways in which the design of processes for back contacts can be optimized.

Even in the best case, interfaces are roughened during the alloying step. Furnace anneals result in standard deviation of junction depth roughly equal to the depth. The smoothest surfaces are obtained by rapid thermal anneal. Short times are adequate to produce a thick recrystallized p+ region at the back of the cell. Stresses caused by the difference in thermal expansion between Al and Si are high (130 MPa for 2 μm Al), and remain high after significant passage of time. Thicker films result in higher stresses. Stress relief is correlated with cracking and delamination of the Al film. It is recommended that higher processing temperatures be used because they result in a thicker p+ region for a given amount of aluminum.

Gettering in solar cells during alloyed backside contact formation can occur in three ways: by liquid phase gettering, by segregation gettering and by outdiffusion of impurities to the surface. Segregation coefficients, k, are calculated for iron in boron-doped silicon as a function of temperature and dopant concentration of the p+ region. For iron in Si with an Al-doped p+ layer, $k \leq 30$. Segregation coefficients increase as temperature decreases and as p+ doping increases. Gettering by outdiffusion occurs by similar processes as haze formation. A pair formation model is used to rank precipitation tendencies based on thermodynamic quantities. Lifetime measurements confirm that gettering is improved as alloying temperature or process time is increased.

Thesis supervisor: Lionel C. Kimerling
Thomas Lord Professor of Materials Science and Engineering

Acknowledgments

I would like to begin by thanking my thesis supervisor, L. C. Kimerling, for his guidance and encouragement. The whole Kimerling group deserves my gratitude for their suggestions, dialog and friendship. In particular I would like to acknowledge Jorg Palm, Jurgen Michel, Anu Agarwal, Gerd Norga, Sang Ahn, Xiaoman Duan, Lee Tatistcheff and Hichem M'saad. Bo Zheng could always point me in the right direction regarding who to talk to at MTL or where I could find the information I was looking for. Laura Giovane was there for talk practice. I haven't mentioned everyone, but they all made a difference in my time here. A thank you should also go to Kate Paterson and Claire Leheny who helped in numerous ways, especially during the last semester when I wasn't always in Cambridge. Discussions with Ilan Blech contributed to my research and the interpretation of results. The NSF should get a mention here, for supporting me for three years.

A big thank you goes to my hosts in Boston over the last semester: Steve and Angela, and Adam and Amy. They more than graciously opened their homes to me.

My parents encouraged me to excel in school and to learn about the world around me. To them I owe a lot. I also thank them for not asking too often when I planned to finish.

Most of all I would like to thank my husband David. He supported and encouraged me throughout the thesis writing stage and listened to things he didn't understand about my work to help me understand them. I am most grateful for his friendship and how it transformed my graduate school experience. I also thank our baby, who kept me awake and cheerful with his kicking.

Dedication

To the One who made this thesis possible:

The day is yours, and yours also the night;
You established the sun and the moon.
It was you who set the boundaries of the earth;
you made both summer and winter.

– Psalm 74:16-17

Table of Contents

List of Figures

List of Tables

Chapter 1

Introduction

Metal-semiconductor contacts are required for the usefulness of devices. High contact resistance and high recombination rates at contacts due to the presence of interfaces restrict device performance. In the case of solar cells, an alloyed backside contact has been shown to improve cell efficiency over cells made with standard (low temperature) contacts. In this introductory chapter the basic function of solar cells is discussed along with the issues involved in aluminum backside contact formation on silicon photovoltaic devices.

1.1 Silicon Solar Cells

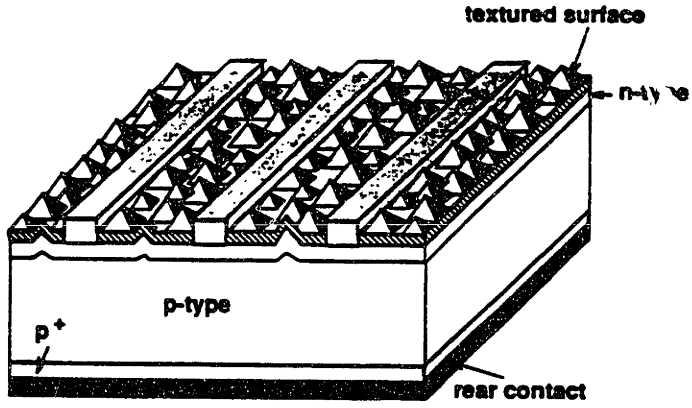

Figure 1.1 A schematic of a typical n-p-p+ solar cell

The basic solar cell, as shown in Figure 1.1, consists of a p-n junction and front and rear contacts. The internal field created by the junction separates electrons and holes excited by absorbed light and collects them into an internal circuit.

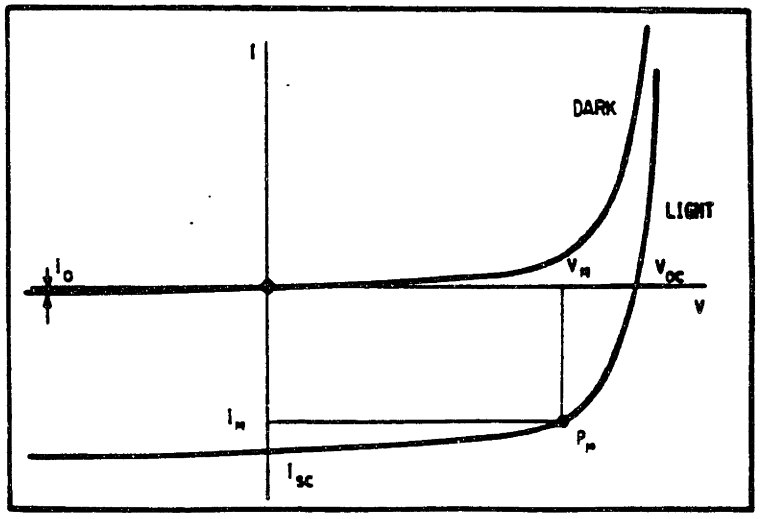

Figure 1.2 Current-voltage characteristics typical of solar cells [1]

The potential difference built up between the two sides of the cell when illuminated in an open circuit condition is referred to as the open circuit voltage, V_{oc}. The value of V_{oc} is constrained by the bandgap ($V_{oc} < E_g$) and depends on the difference in doping between n- and p-type regions that form a homojunction. Another important parameter is J_{sc}, the short circuit current density. In a solar cell it can be defined as the reverse light-generated current density when the cell is illuminated in a short circuit condition. The value of J_{sc} depends on the effectiveness with which the junction collects electrons and holes created by absorbed photons before they are lost to bulk or surface recombination. Recombination centers are associated with defects such as impurities, dislocations and grain boundaries. J_{sc} also depends on the intensity and spectral distribution of the incident light. In the ideal case the short circuit current is equal to the light generated current, I_L, and V_{oc} would be given by

$$V_{oc} = (kT/q)\ \ln[I_L/I_o + 1] \qquad (1.1)$$

where k is the Boltzmann constant and q is unit charge. Saturation current density, I_o, is inversely related to minority carrier diffusion length and to dopant concentration. There is a positive relationship between carrier diffusivities and I_o. In the actual case, I_L in the above equation is replaces by I_{sc}, the short circuit current.

The fill factor, FF, is a measure of the squareness of the illuminated I-V curve. It reflects the obtainable power from a cell and is given by

$$FF = P_m/(V_{oc}\, I_{sc}) \tag{1.2}$$

where P_m is the maximum power. Cell efficiency, in turn, is given by

$$\eta = P_m/P_{in} = (V_{oc}\, I_{sc}\, FF)/P_{in} \tag{1.3}$$

if P_{in} represents incident solar power.

Carrier lifetimes, τ, are inversely proportional to recombination velocities and are related to the diffusion length by $L = \sqrt{D\tau}$. Recombination processes include radiative recombination, Auger recombination and recombination due to impurity traps and traps at surfaces. Of particular interest are the traps associated with impurity or defect states in the bandgap. Transition metal atoms and surfaces are particularly effective recombination centers. Effective surface recombination velocity is denoted S_{eff} and reflects the number of trap states at a surface. Surface recombination is the dominant mechanism for efficiency loss. Cell efficiency could be improved by reducing the number of these traps. Thinner cells result in lower recombination rates, but absorption of incident light and mechanical strength become issues.

Device design consists of the optimization of material choice and processing so that efficiency and reliability are maximized while cost is minimized. The cell ought to be capable of collecting more useful energy than went into its production with minimal environmental impact. This calls for simple processes. Silicon is chosen as a photovoltaic material because it offers advantages including material abundance, an established technology base, high quality and good surface passivation characteristics (with its oxide) [2]. Its major drawback is that it is an indirect bandgap material, making solar energy conversion less efficient.

1.2 Alloyed Contacts

An alloyed contact is formed by depositing a metal onto a semiconductor substrate and annealing at a temperature high enough to form a eutectic liquid. If aluminum is

deposited on Si, the temperature must therefore exceed 577°C, the eutectic temperature of the system. Upon cooling, some of the silicon taken into the melt recrystallizes, doped to the solubility limit with the metal. This recrystallization continues until the eutectic point is reached, at which point the rest of the liquid solidifies together. The result is a structure, shown schematically in Figure 1.3.

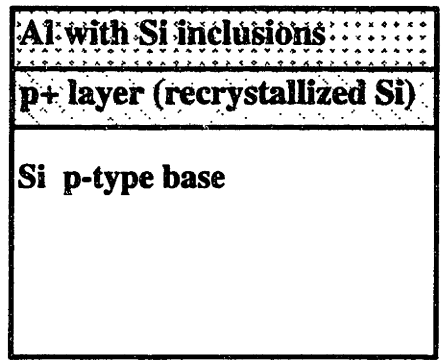

Figure 1.3 Schematic of alloyed junction structure

Occasionally the alloying procedure is incorrectly referred to as diffusion. Some diffusion of Al into the Si substrate can occur during the alloying process, but diffusion depth is insignificant compared to the doping caused by recrystallization of aluminum doped silicon. For example, at 850°C Al is expected to diffuse to a depth of 0.02 microns during a 30 minute anneal. Typical thickness of the recrystallized layer is at least one micron, and usually higher.

Alloyed junctions were first used in silicon technology for integrated circuits. While the high doping underneath the contacts resulting from this process was advantageous, the method was dropped due to difficulties with reproducibility and uniformity. The technology became impractical as demands on device performance increased. These are the same issues facing solar cell manufacture today. The alloyed junction has survived in solar cells because, despite the deleterious effects of the process such as surface roughening and nonuniformity of the p-p+ junction, the overall effect on

cell efficiency is positive. Note also that the Al-Si combination is not the only one possible. Al doped with B is sometimes used to form an even higher doped p+ layer because B has greater solubility in Si. [3] Alloyed junctions are also used in compound semiconductor systems.

1.2.1 Alloyed Backside Contacts for Silicon Solar Cells

The benefit of using alloyed backside contacts has been known for many years. The treatment results in improved open circuit voltage, short circuit current density and cell efficiency. Alloying has resulted in a 5-10% improvement in the efficiency of cells made on 10 Ωcm p-type substrates. [4] The effect was first attributed to gettering of impurities from the bulk [5] and then it was thought that the influence of the heavily doped region at the back was the reason for improved performance. [6, 7, 8] Both the gettering effect and the back surface field (BSF) effect have been shown to be important.

What is termed the back surface field effect is the reduction in effective surface recombination velocity, S_{eff}, at the rear contact. In the region heavily doped with Al, the flow of minority carriers (electrons) to the back contact is restricted to the larger than usual negative charge of the acceptors in the contact area. With fewer minority carriers in the vicinity of the contact, recombination is reduced. As a result voltage output of the cell is increased. For the BSF cells described here a typical value for S_{eff} at the backside contact is 1000 cm/s. Without the alloyed backside contact S_{eff} would be on the order of 10^7 cm/s. It is still true that recombination is dominated by recombination at surfaces, especially at the contacts. [5, 9]

For best results in controlling S_{eff} the p+ region should be uniform; however, it is known that surface roughening accompanies the alloying procedure. King, et al. suggest that spiking occurs during processing. [10] Selective dissolution of Si in Al during the alloying step is the suggested cause for surface roughness of del Alamo, et al.. [11] The results of this work suggest the latter, and that annealing conditions can be controlled to minimize roughening. These results are given in Section 2.2.1.

During the formation of an alloyed metal contact, there is an opportunity for impurities to diffuse to the molten alloy and be held there as the metal cools. This is one way gettering can occur in BSF solar cells and is the result of high solubilities of impurities in aluminum compared to silicon. "Back surface field-induced" gettering has been shown to exist for various treatments with B and Al such as ion implantation and doped silica-film deposition followed by an anneal. [12] Such results are significant because they show gettering independent of the molten metal layer.

Additional advantages of producing a backside contact in this way are listed by Wohlgemuth and Narayanan. [13] The doping of the backside with Al offsets the possibility of forming a back p-n junction during the earlier P diffusion (to form the cell junction.) It is also during the alloying step that ohmic contact is established with the rear of the cell, making for a simple process.

1.2.2 Processing of BSF Cells

One goal of this thesis is to define the conditions that contribute to improving cell efficiency so that optimum processing conditions can be defined in general. Much of the previous work on Al backside alloyed contacts for Si photovoltaics has concentrated on optimizing the process for a specific cell design. The variables have been deposited Al thickness, alloying time and temperature. The relationship of these parameters to others in the cell design is not considered. As a result many apparently conflicting results have been obtained. The issues are complicated in that most solar cells are made on polycrystalline silicon, in which case grain boundary effects should be considered.

Reported processing schemes include T's from 650° to 1200°C and processing times from 30 seconds (for rapid thermal annealing) to several hours. The most common temperatures are between 750 and 950 degrees. Usually, process optimization is done for a given solar cell structure. It is not surprising that results depend on factors other than the rear contact processing alone.

The backside contact is formed in one of the last steps. Commonly Al is deposited by screen printing an aluminum paste onto the back of the cell. This results in a somewhat

different structure of the metal, as compared to evaporative or sputter deposited films, because of outgassing of organic binders during the high temperature step.

The thickness of the highly doped region is relevant to performance. Lölgen has modeled the relationship of surface recombination velocity to BSF thickness, finding that as thickness increases, the S_{eff} is lowered. He also reports that for a given BSF thickness, the doping of the region is important. Higher doping of the p+ region is expected to reduce S_{eff}, reaching a minimum at about 5×10^{19} cm^{-3}. [14]

In this work all experiments are done using single crystalline CZ or FZ silicon wafers. To ensure that all observed effects are due to the alloying step, no other processing was performed on the wafers. Aluminum was deposited by e-beam evaporation. Furnace anneals were carried out at temperatures ranging from 850°C to 1050°C, and rapid thermal annealing was done at 950°C and 1000°C. The annealing ambient is either nitrogen or argon. Time at the alloying temperature is varied.

Good sources for general solar cell information are the books by Green [15, 16] and the book by Hu and White [17].

Chapter 2

Backside Contact Metallization

Alloyed backside contacts are used in the manufacture of silicon solar cells because of their positive effect on cell efficiency. This chapter details the results of work done with the goal of illuminating the physical processes behind the observed performance improvement.

2.1 Aluminum-Silicon Phase Equilibria

The phase equilibria between the two elements is the basis of understanding the contribution of alloyed Al backside contacts to silicon solar cell performance. Figure 2.1 is the Si-Al phase equilibrium diagram.

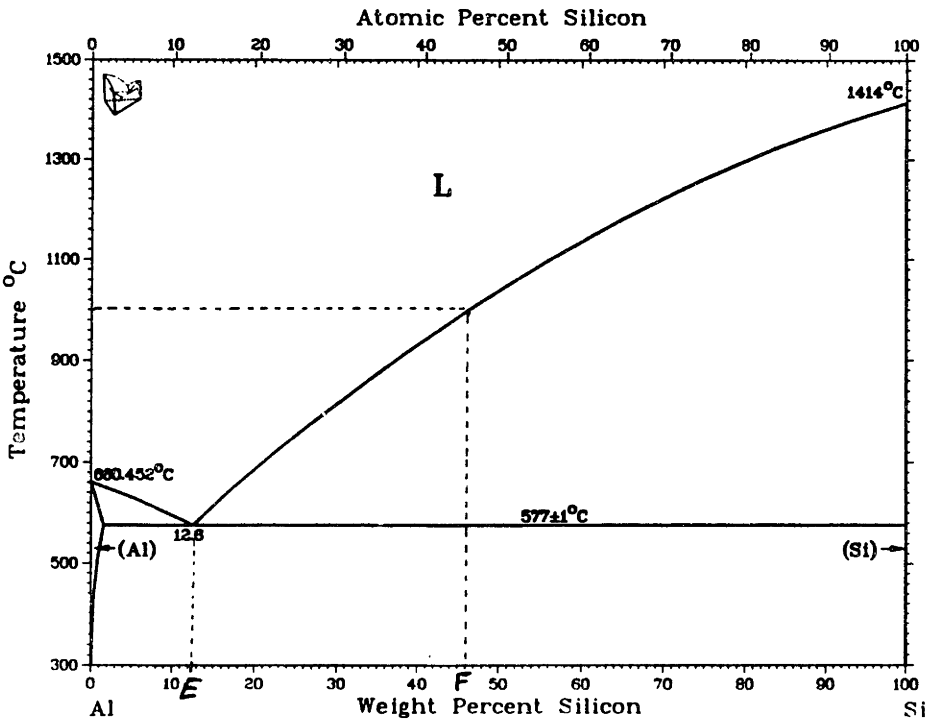

Figure 2.1 The Al-Si phase diagram [18]

During the alloying step temperatures exceed the Si-Al eutectic. This means that the Si beneath the metallization is brought into the melt during the high temperature step.

The amount of Si dissolved depends on the processing temperature and is proportional to the aluminum thickness. This relationship can be derived from the phase diagram. [11] At the annealing temperature, T, the melt should have a composition given by F, the composition of the point on the liquidus corresponding to annealing temperature. (See Fig. 2.1.) The amount of Si that must melt to reach this composition can be calculated for a given thickness of Al.

$$wtAl = t_{Al}\,\rho_{Al} \tag{2.1}$$

per unit area where wtAl is the weight, t_{Al} is the thickness, and ρ_{Al} is the density of aluminum. The weight of silicon brought into the melt is given by

$$wtSi = t_{Si}\,\rho_{Si} = [F/(100\text{-}F)]\ wtAl = t_{Al}\,\rho_{Al}\,[F/(100\text{-}F)] \tag{2.2}$$

where t_{Si} is the thickness of silicon brought into the melt. Thus,

$$t_{Si} = (t_{Al}\,\rho_{Al}/\rho_{Si})\,[F/(100\text{-}F)] \tag{2.3}$$

On cooling, the composition of the melt changes from F to E for $T>T_e$. It is during this cooling that Si recrystallizes, doped to the solubility limit with Al, and forms the p+ layer. The remaining Si in the melt solidifies with the Al at the eutectic temperature. So, the weight of the Si included in the eutectic is [E/(100-E)] wtAl. This expression gives the thickness of the recrystallized Si to be

$$t_{Si\,r} = (t_{Al}\,\rho_{Al}/\rho_{Si})\,[F/(100\text{-}F) - E/(100\text{-}E)] \tag{2.4}$$

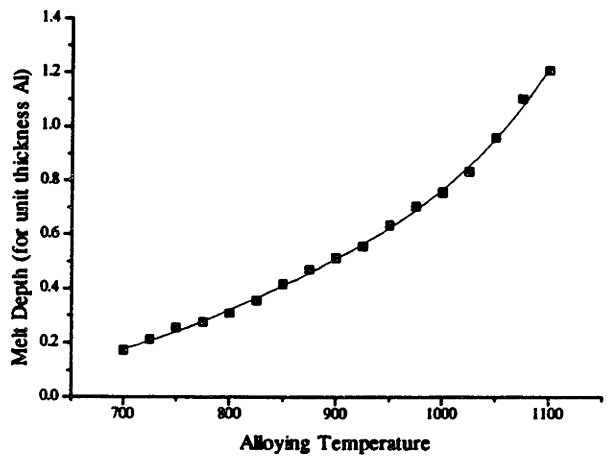

Figure 2.2 Theoretical curve relating deposited Al thickness and melt depth as a function of alloying temperature (in °C).

From Equation (2.4) we get the relationship between Al thickness and theoretical junction thickness shown in Figure 2.2. This assumes that there is no diffusion of Al into the solid Si and that the interfaces are planar. It is clear from these results that the lower the processing temperature, the thicker the deposited Al layer must be to achieve the same p+ layer thickness.

2.2 Alloy Junctions

It is desired that we compare the results of Section 2.1 to what is found experimentally. In the following sections the actual interface morphology and doping of the recrystallized region are considered.

2.2.1 Interface Morphology

We have chosen to use microscopy to study the interface morphology and structure of the highly doped region beneath the alloyed contact. Scanning electron microscopy (SEM) was used to examine the eutectic structure on the rear of the cell. N-type wafers were subjected to various alloying treatments so that electron beam induced current (EBIC) could be used to view the p-n junction formed during processing. By combining secondary electron images and images obtained by EBIC, junction depth and uniformity could be shown.

Figure 2.3 is a cross sectional view of the contact area, showing the eutectic structure and film roughens. Figure 2.4 is a cross sectional view of the contact region on a (111) wafer. It is observed that faceting along (111) planes occurs during the alloying step. This indicates that alloyed junctions formed on (111) wafers could be more uniform than those on (100) substrates. Significant nonuniformities, however, are still found in this case.

A combined EBIC-SEI image is shown in Figure 2.5. The structure shown here is formed by alloying a 2 micron thick layer of Al on an n-type wafer at 950°C for 30 minutes. The resulting p-n junction appears in the image as a bright line. For this sample average junction depth was measured from the images to be 1.8 microns, slightly greater

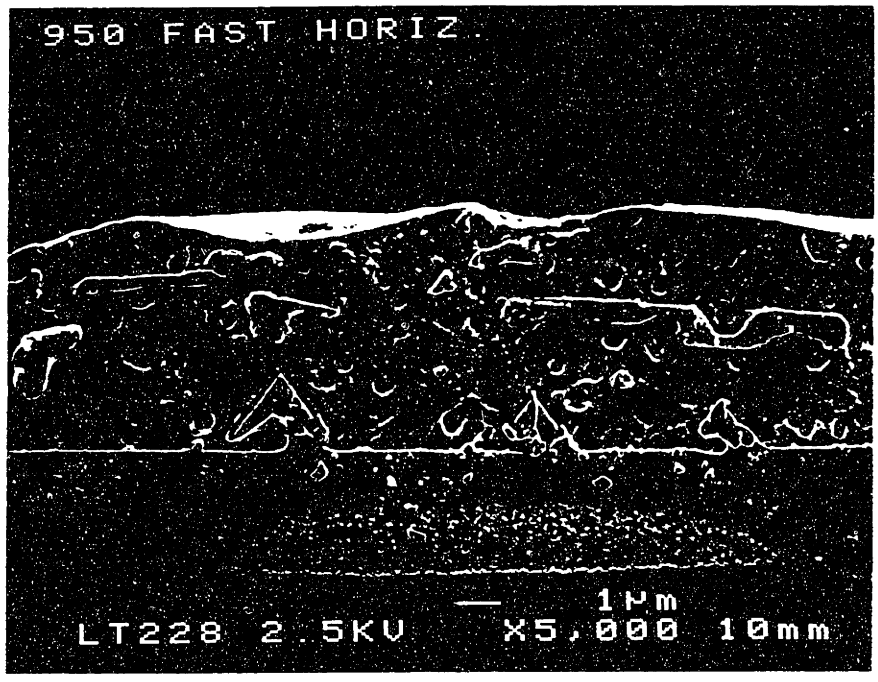

Figure 2.3 SEM micrograph of the contact area showing eutectic structure on a (100) wafer. This sample was prepared by annealing at 950°C for 30 minutes in nitrogen.

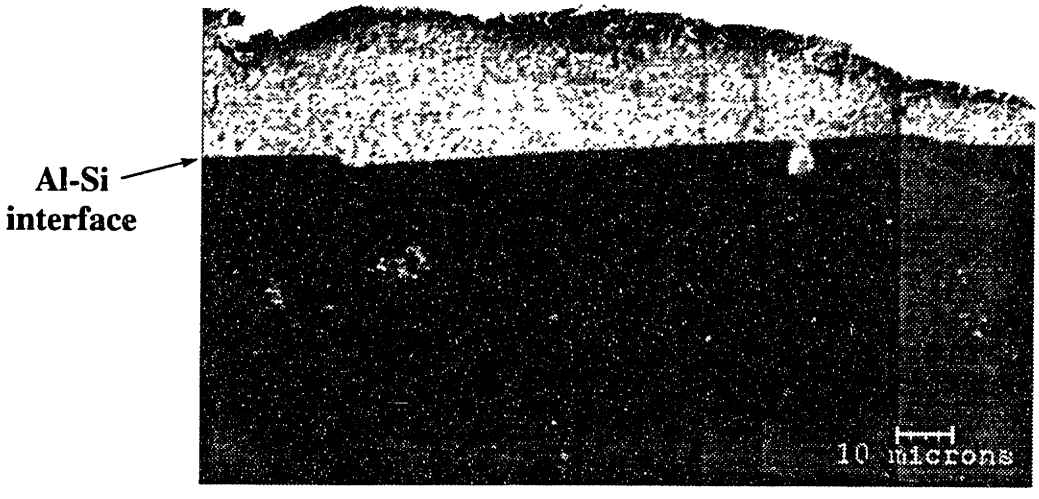

Figure 2.4 SEM micrograph showing a cross sectional view of the contact area on a (111) wafer. Processing was at 850°C for 30 minutes. Notice step formation and pitting along (111) planes.

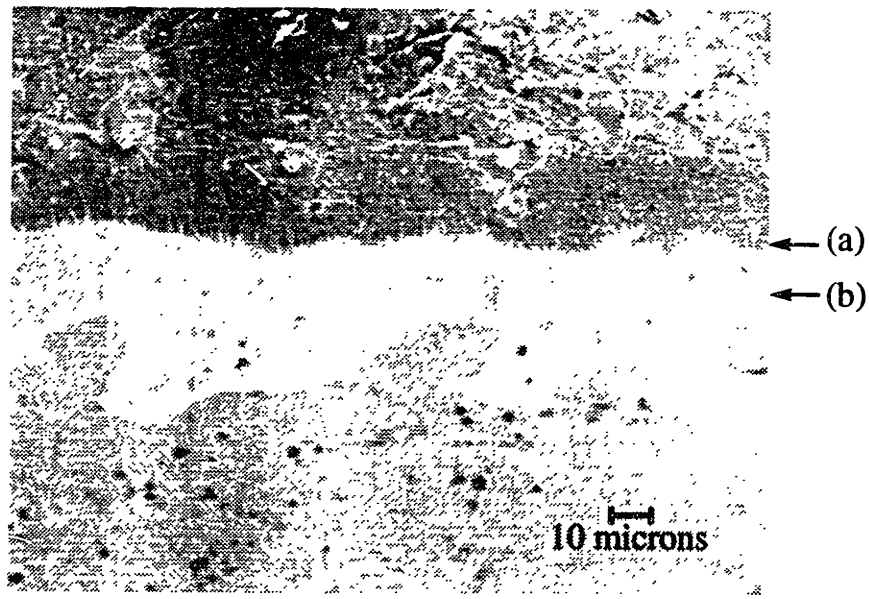

Figure 2.5 Combined EBIC-SEI image showing the junction formed by alloying for a furnace annealed sample (950°C for 30 minutes.) The sample is beveled at 4 degrees and shows the Al-Si interface (a) and the p+-n junction (b).

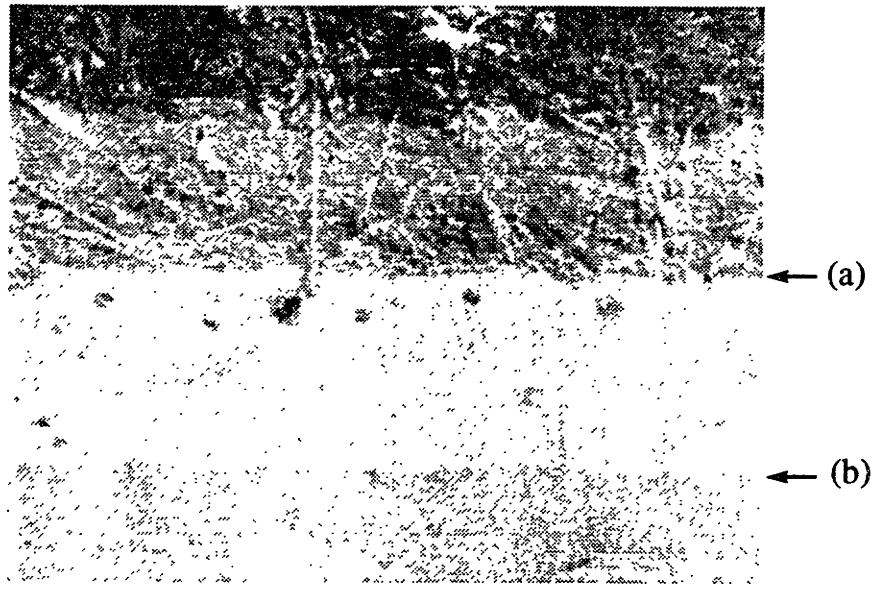

Figure 2.6 Image showing the junction formed by alloying for a rapid thermal annealed sample (1000° for 10 seconds) The sample is beveled at 4 degrees and shows the Al-Si interface (a) and the p+-n junction (b).

than that predicted from Equation (2.4). However the error in this value is quite large (on the order of the thickness itself,) not allowing for meaningful comparison. Note that in general the junction follows crystallographic directions, suggesting preferential melting along (111) planes. For all furnace annealed samples observed, similar roughness of interfaces and junctions was seen regardless of processing time or temperature. Nonuniformities can be caused by thermal instabilities or dirty interfaces.

The appearance of furnace annealed samples contrasts with that of rapid thermal annealed samples. RTA results in much smoother interfaces and junctions, though roughness is not eliminated. Figure 2.6 shows a beveled sample with a 2 μm layer of Al, annealed at 1000°C for 10 seconds. Even this time is sufficient to create a thick p+ layer, measured to be 3.0 μm. The reason the melt interface, revealed by EBIC as a p-n junction, is more uniform for RTA samples is probably related to the rapid rise in temperature not possible in a furnace. When this occurs, the system becomes superheated resulting in a greater number of melt nucleation sites over the substrate surface. The measured melt depth is much thicker than the phase diagram would suggest.

The roughness observed here reduces the effectiveness of the backside field in retarding surface recombination. Because rapid thermal annealing produces the most uniform results, it is the best alloying method in this sense. If gettering optimization would benefit from longer anneals, a rapid thermal anneal at high temperature could be followed by a lower temperature furnace anneal, where the Al-doped silicon would not all be brought back into solution. In this case the even p-p+ junction should remain.

It has previously been reported, or simply assumed, that the thickness of the recrystallized layer is the theoretical one. (See for example del Alamo. [11]) This has clearly been shown not to be the case, for reasons of roughness and nonequilibrium effects.

2.2.2 Doping

The doping of the p+ layer was determined by spreading resistance. it was approximately 4 x 10^{18} cm^{-3}, slightly below the solubility of Al in Si at the processing

temperature. This measurement was performed on a (111) p-type wafer, doped at 10^{15} cm^{-3}, deposited with 2 mm Al and annealed at 850°C for 30 minutes. The presence of a n-p+ junction was confirmed in the case of n-type wafers with an alloyed Al contact. Doping densities measured for these wafers by spreading resistance were also as expected. Figure 2.7 is a detail of the phase diagram, showing the solubility of Al in Si as a function of temperature.

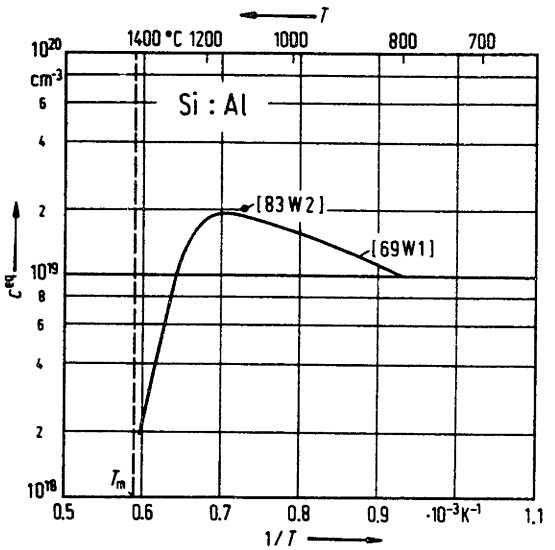

Figure 2.7 Solubility of aluminum in silicon as a function of temperature [19]

There is no evidence that Al doping densities follow a trend given by equilibrium considerations. Even moderately rapid cooling results in doping densities that correspond to solubility at the processing temperature. This is a desirable effect, providing more uniformly doped layers.

The junction depth for the above sample is 1.8 microns. This corresponds to average values for wafers processed under the same conditions measured by EBIC. It is clear that spreading resistance yields an average value, given the interface roughness observed by electron microscopy. Because of the severe nonuniformity of the p+ layer, it is also possible that errors in measured doping level result from this technique.

2.3 Process-Induced Stress

Differences in the coefficient of thermal expansion of silicon and aluminum cause the Al to be in tension after cooling to room temperature. The thermal expansion coefficients for Al is 23.1 x 10^{-6} $°C^{-1}$, compared to a value of 2.6 x 10^{-6} $°C^{-1}$ for Si. Once the Al has solidified following the alloying step, thermal stresses begin to build up. Thermal stress is given by

$$\sigma_{th} = \left(\frac{E_s}{1-\nu_s}\right)\Delta\alpha\Delta T \tag{2.5}$$

where E_s is the elastic modulus of the substrate, ν_s is Poisson's ratio of the substrate, $\Delta\alpha$ is the difference in linear coefficients of thermal expansion and ΔT is the temperature change. The stress is clearly thermal history dependent, not only because of the build up of stress due to differences in thermal expansion, but also because at higher temperatures Al is likely to flow plastically, allowing for stress relief.

2.3.1 Method of Stress Measurement

In response to stress caused by a film, a substrate will elastically deform to reach a minimum energy configuration. Stress was monitored using a laser scanning system which measures changes in radius of curvature. A schematic of the apparatus is shown in Figure 2.8.

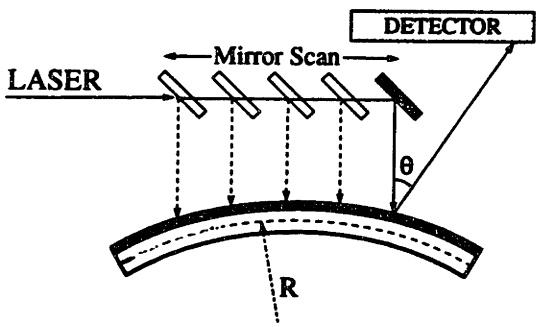

Figure 2.8 A schematic of the scanning laser stress measurement system

Average stress is related to curvature by the Stoney equation [20]

$$\sigma = \frac{E_s h^2}{(1-\nu_s)6t} \frac{(R_1 - R_2)}{R_1 R_2} \tag{2.6}$$

where h is the substrate thickness, t is the film thickness, R_1 is the radius of curvature of the substrate prior to Al deposition and R_2 is the radius of curvature after processing. It is only necessary to know the elastic properties of the substrate and film and the substrate thickness to measure stress. No knowledge of the microstructure of the film is needed to carry out these measurements.

2.3.2 Measurements and Observations

Immediately after processing, measured stresses are substantial. For wafers with 2 microns Al, these are greater than 130 MPa. As shown in Figure 2.9, the initial decrease in stress is rapid and the average stress drops to approximately 100 MPa in 24 hours. Micrographs show that accompanying this stress relief is a change in microstructure that includes cracking and delamination of the Al film. See Figure 2.10 for an example of the cracking behavior. In the long term, even after 6 months, stresses of 60 MPa are maintained. It was also found that the stress level correlates with the thickness of the Al layer.

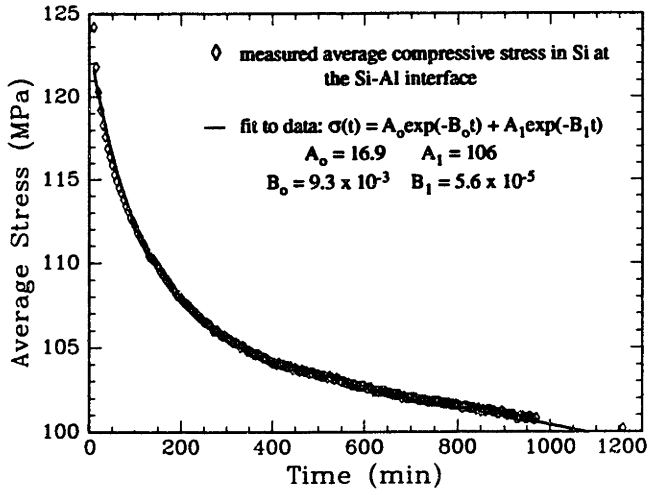

Figure 2.9 Stress relaxation at room temperature after alloying step for a (100) wafer with 2 microns Al

Thermal cycling results in stress relief on heating followed by restoration to nearly the previous value upon subsequent cooling. (Figure 2.11) Curves follow behavior usually found for aluminum films on silicon substrates, with a slope of the cooling curve of 1MPa/s Apparently the effect of Si inclusions in the Al film on mechanical properties of the metal is minimal.

Stress may influence the redistribution and precipitation of impurities. Because the Al is in tension, the backside of solar cells are in compression, inhibiting diffusion there. The tensile stress of the aluminum contact works to keep transition metal impurities in the Al layer. Stresses do not start to build until below the eutectic temperature, so at higher temperatures redistribution of impurities is not affected. Stress also influences the precipitation of impurities. Precipitation would be enhanced if the change in volume to the precipitate is negative, and hindered if the precipitate has lattice constants larger than that of the unstrained Si lattice. Mechanical strains do have an influence in the gettering process by affecting the critical size of precipitates and the co-precipitation process due to elastic strain compensation. [21]

Stress can be minimized in two possible ways. First, slow cooling below the eutectic would allow plastic flow of Al and prevent large stresses from building in the film. Stress cannot be eliminated this way, but can be reduced if the cooling schedule is compatible with other process considerations. Secondly, higher processing temperatures rather than thicker aluminum layers should be used to produce thick p+ layers. Higher doping of the recrystallized silicon would also result.

2.4 Other Reactions During Alloying Step

The alloying step is commonly carried out in a nitrogen atmosphere. The original patent on the BSF process assumes that nitrogen is an inert gas. [22] This is not the case at elevated temperatures. In fact, we have found that after high temperature anneals or long times at lower temperatures, there is nitride present in the metal film. X-Ray diffraction shows peaks associated with AlN. When this compound forms it reduces the conductivity of the backside contact layer. As a result, the alloying step should either be

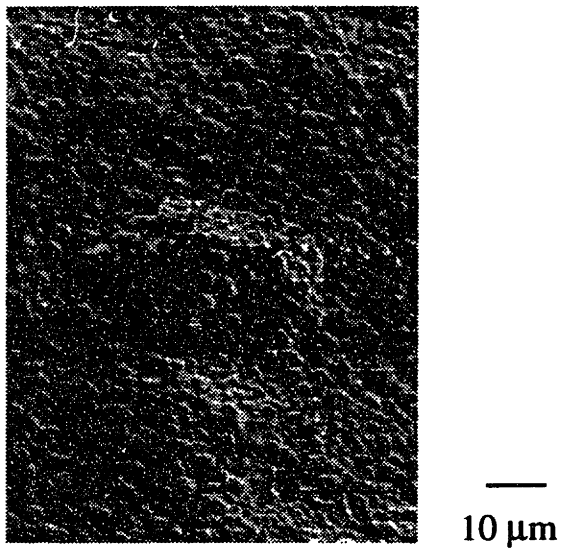

Figure 2.10 SEM micrograph showing cracking of the Al film 24 hours after processing

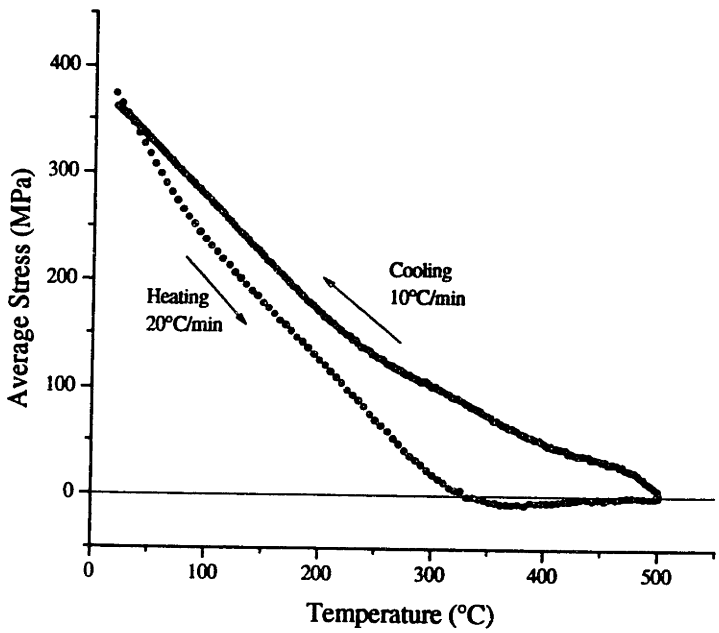

Figure 2.11 Stress variation in alloyed Al on Si caused by thermal cycling. For this wafer aluminum thickness is 3.5 microns. The temperature was held at 500°C for 15 minutes.

performed in argon or in nitrogen under conditions which do not permit appreciable formation of nitride.

It is suggested by Joshi, et al. that annealing in an N_2 ambient alone results in gettering. [23] Since they did not compare their results to annealing alone in other atmospheres, it is possible that the observed improvement in lifetime is due to outdiffusion in general and does not require the presence of nitrogen.

There is evidence that gettering occurs during the alloying step. This will be discussed in greater detail in Chapters 3, 4 and 5. Improvements to minority carrier lifetime will be discussed in Chapter 6.

Chapter 3

Gettering of Transition Metal Impurities

This chapter provides a basic introduction to the issues related to gettering associated with alloyed backside contact formation.

3.1 Overview

Gettering is the process of removing or controlling electrically active defects to improve electrical performance in the active regions of a device. The processes involved are as follows: (i) the release or dissolution of contaminants in the device area, (ii) diffusion of contaminants, and (iii) the stable capturing of the contaminants at given sites. It is important to maintain the stability of the last step in later processing steps since the gettering process can be reversible. Gettering processes for solar cells must take into account that bulk properties determine device characteristics. Thus gettering to surfaces is desirable.

Possible gettering sites include dislocations, oxygen precipitates and grain boundaries in addition to surfaces. Regions of higher defect solubility are also candidates because a chemical gradient results in diffusion to these locations. Gettering by this mechanism is termed segregation gettering.

Gettering may occur when supersaturated species precipitate out of solution. This mechanism requires sufficient mobility of defects to either internal or external gettering sites. Internal sites may be dislocations or oxides, whereas the external site is usually the back surface. This type of process may occur during cooling from high temperature, or during low temperature processing steps.

Haze is the near surface precipitation of metallic impurities and forms during cooling from high temperatures as the supersaturated species outdiffuses and precipitates. Studying haze can illuminate factors governing gettering to wafer surfaces because it occurs by the same mechanisms.

When there is a gradient in chemical potential gettering can occur. This may happen during high temperature treatment when the gettering zone offers a higher effective solubility. Because it happens at high temperature, this gettering mechanism is especially useful for slower diffusing species. The possibility of gettering iron by diffusion to a highly doped p-type region is discussed in Section 4.4. This is possible because the solubility of iron depends on dopant concentration.

For a complete understanding of gettering the following issues should be understood: solubility and diffusivity of impurities, reversibility of processes, influence of point defect injection (important in gettering associated with P diffusion, for example), effect of local strains, metal-dopant complexing and the effect of interfaces. Competition of gettering sites should be considered. Processes should be designed so that the most favorable sites are those to which you want defect species to go. For a more complete discussion of issues related to gettering consult Graff [24] or Kang and Schroder [25] among other sources.

In the case of gettering associated with backside contact formation, several mechanisms are operational. Segregation gettering takes two forms: Gettering to the liquid phase and to the p+ recrystallized region. Outdiffusion and surface precipitation occurs upon cooling. Liquid phase gettering is discussed in Section 3.2. Modeling of the solubility enhancement of Fe in highly doped p-type silicon provides a basis for understanding segregation to p+ regions. This is covered in Chapter 4. Chapter 5 is concerned with developing an understanding of haze formation. This is used as a basis for thinking about outdiffusion and precipitation of metals.

3.2 Liquid Phase Gettering

An evaporated aluminum layer is known to getter copper and nickel from Si below the Al-Si eutectic. [26] Sana, et al. propose that pitting or damage of the Al-Si interface provides gettering sites. [27] At temperatures above T_e it is expected that liquid phase gettering can occur because the liquid has high metal solubility. Gettering by this mechanism occurs by diffusion of impurities from the back to the rear contact during

alloying. Apel et al. studied the aluminum gettering of cobalt in Si finding a 90 percent reduction in Co concentration after alloying for 30 minutes at 820°C. [28] From this they derive a segregation coefficient $k = [Co]_{AlSi\,l}/[Co]_{Si\,s}, = 10^4$, where $[Co]_{AlSi\,l}$ and $[Co]_{Si\,s}$ are the cobalt concentration after gettering in the Al-Si layer and Si, respectively. This figure agrees with predictions of segregation coefficient based on equilibrium metal solubility. [23] These results suggest that liquid phase gettering is the predominant mechanism of gettering associated with alloyed backside contacts.

Chapter 4

Modeling Solubility of Transition Metals

Because dissolved metals are charged species, solubility may be enhanced or diminished by the presence of dopant atoms. This section describes a model developed to calculate solubility based on dopant concentration. This model differs from previous calculations in that Fermi statistics are used to calculate the fraction of iron ionized at high temperatures. Due to the broadness of the Fermi function at elevated temperatures, a significant portion of iron remains charged. Thus, solubility enhancement at high doping levels is shown to exist, even at high temperature. The results include the calculation of the segregation coefficient of iron between p and p+ regions and the effect of doping and treatment temperature on carrier lifetime at room temperature.

4.1 Background

Transition metal contaminants in Si, introduced during high temperature processing, have a negative impact on cell performance. Processing temperature or base doping determines the effect of metals because these factors influence solubility, equilibrium defect states and thereby carrier lifetime. Here, iron is chosen as a representative fast diffusing impurity because it is a common contaminant in semiconductor manufacture. Its solubility is modeled as a function of boron concentration in a manner similar to that followed by M'saad. [29] Processing temperature is relevant as it dictates intrinsic solubility.

For the case of a boron doped substrate with iron impurities, the following are the equilibrium ionization reactions:

$$Fe_{(ext)} \rightarrow Fe_{i(Si)} \tag{4.1}$$

$$Fe_i \rightarrow Fe_i^+ + e^- \tag{4.2}$$

$$B_s \rightarrow B_s^- + h^+ \tag{4.3}$$

$$e^- + h^+ \leftrightarrow [\text{bond}] \tag{4.4}$$

Electroneutrality must be maintained so that, assuming there is no pairing at high temperature

$$[B_s^-] + n = [Fe_i^+] + p \tag{4.5}$$

Applying the law of mass action, the equilibrium of (4.1) is driven to the right by electron-hole recombination (4.2). Because acceptors provide holes, the solubility of donors in Si increases with boron concentration. Combining the above equations, we obtain

$$[Fe^+] = C\,p \tag{4.6}$$

where C is a constant, for constant external iron activity. Reiss observed similar behavior for Li in p-type Si. [30] Note that if there was an n-type donor, the solubility of iron would decrease with dopant concentration because the donor ionization reaction liberates an electron, inhibiting the iron ionization reaction.

At high temperature, the ionization of iron is not complete because the Fermi level approaches midgap as the intrinsic carrier concentration exceeds doping levels. The total iron concentration is simply given as the total of the concentration of charged and uncharged iron species. Following the analysis of Reiss, the concentration of positively charged iron is related to acceptor concentration as follows

$$[Fe^+] = \frac{N_a}{1+\sqrt{1+\left(2n_i/[Fe^+]^o\right)^2}} + \sqrt{\left(\frac{N_a}{1+\sqrt{1+(2n_i/[Fe^+]^o)^2}}\right)^2 + \left([Fe^+]^o\right)^2} \tag{4.7}$$

where $[Fe^+]^o$ is the maximum equilibrium concentration of positively charged iron when [B]=0, N_a the boron (or acceptor) doping density, and n_i is the intrinsic carrier concentration. In the model, values for $[Fe^+]^o$ are obtained using Fermi statistics and the following expression for equilibrium solubility of iron in Si for lowly doped material (N_a = 10^{13} cm^{-3}.) [31]

$$C_s^o = 5 \times 10^{22} \exp(8.2 - 2.94\text{eV}/kT)\ (cm^{-3}) \tag{4.8}$$

Fermi statistics imply the following relationship

$$[Fe^+] = [Fe]/\{1 + 2\exp((E_f - E_{Fe})/kT))\} \tag{4.9}$$

The intrinsic carrier concentration is given by $n_i = (N_c N_v)^{1/2} \exp(-E_g/2kT)$ where $N_c(T)$ = 3.22×10^{19} $(T/300)^{3/2}$ is the density of states in the conduction band (in cm^{-3}); $N_v(T)$ =

$1.83 \times 10^{19}\ (T/300)^{3/2}$ is the density of states in the valence band, and $E_g(T) = 1.17 - (4.73 \times 10^{-4}\ T^2)/(T+636)$ is the energy gap of silicon in eV. [32]

For the temperatures considered here it is true that $2n_i/[Fe+]^\circ >> 1$ so that

$$1+\sqrt{1+(2n_i/[Fe^+]^\circ)^2} \approx 2n_i/[Fe^+]^\circ \tag{4.10}$$

Thus, equation (4.7) can be simplified to

$$[Fe^+] = \frac{N_a}{(2n_i/[Fe^+]^\circ)}\left[1+\sqrt{1+4(n_i/N_a)^2}\right] \tag{4.11}$$

With this equation the solubility can be calculated as a function of doping density. The results are then used to determine room temperature properties.

4.2 Modeling Solubility

The model of iron contamination of boron-doped Si assumes that the bulk solubility limit is reached during a high temperature processing step. The sample is then instantaneously quenched to room temperature. At room temperature, iron pairs with boron so that equilibrium concentrations of Fe^+ and Fe_iB_s are reached. The pairing reactions are assumed to occur much more rapidly than either precipitation or outdiffusion. At high temperatures, the fraction of ionized iron is calculated based on the assumption that the bulk solubility values reported in the literature reflect total iron concentration, and that the defect level associated with the iron interstitial remains in the same relative position within the bandgap regardless of temperature.

As the temperature and intrinsic carrier concentration increase the Fermi level moves towards midgap. As this occurs the ratio of charge states of the metallic impurities shifts, as the Fermi level sweeps past the impurity level. Table 4.1 lists the percentage of Fe in the Fe^+ state given by Equation (4.9) at various temperatures for low doping ([B] < n_i.) Recall that if the Fermi level is below the defect level the majority of Fe is positively charged whereas if the Fermi level is above the defect level the majority of Fe is neutral. Note that at high temperatures a significant portion of the iron is charged even though the Fermi level is above the defect level. Because this is the case, it is expected that dopant concentration has an effect on iron solubility.

Table 4.1 Summary of parameters needed to model solubility enhancement

T	E_g (eV)	$E_g/2$	n_i	E_{Fe}	$Cs°=[Fe]_{total}$	$[Fe^+]°$
700	0.892	0.446	6.94×10^{17}	0.31	1.08×10^{11}	9.82×10^{9}
900	0.810	0.405	3.41×10^{18}	0.28	4.26×10^{13}	5.96×10^{12}
1000	0.768	0.384	6.41×10^{18}	0.27	4.18×10^{14}	6.14×10^{13}
1100	0.726	0.363	1.10×10^{19}	0.25	2.94×10^{15}	4.84×10^{14}

Using Equation (4.11) and the previously tabulated values, the relationship of doping density to $[Fe^+]$, $[Fe°]$ and total iron solubility were calculated.

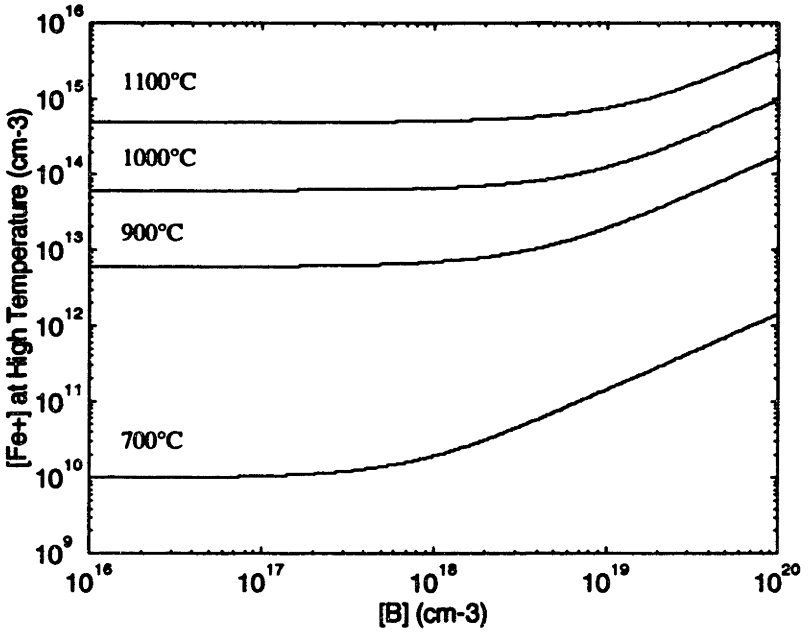

Figure 4.1 Variation of the maximum concentration of Fe+ in Si with boron concentration at different heat treatment temperatures

At low doping densities, where $N_a<n_i$, the material behaves intrinsically and there is no effect of doping on Fe solubility. When $N_a>n_i$, $[Fe^+]=[Fe^+]°N_a/n_i$ and Equation 4.7 reduces to that of a straight line with slope $[Fe^+]°/n_i$. These two regimes can be clearly seen in Figure 4.1. Figure 4.2 shows the relationship of doping density to total iron concentration.

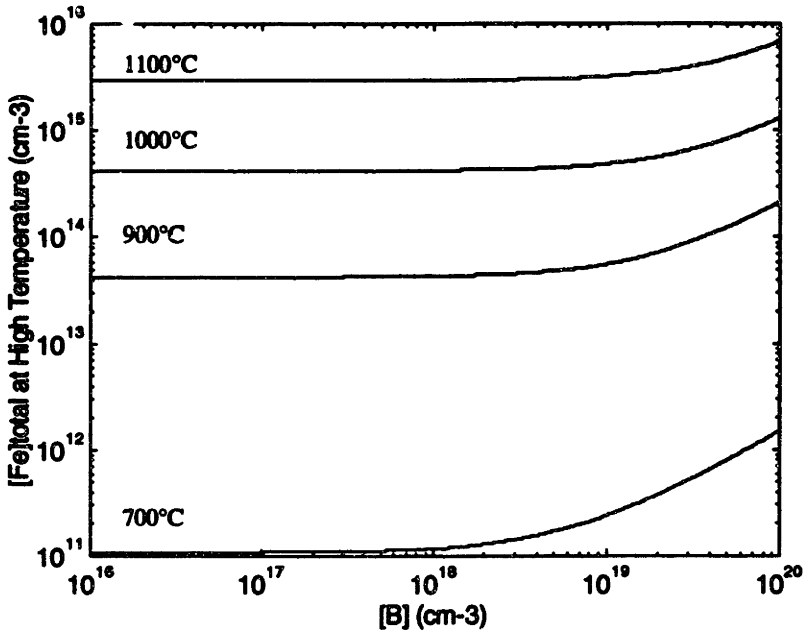

Figure 4.2 Variation of the solubility of Fe with [B] in boron-doped Si at different heat treatment temperatures

4.3 Redistribution of Fe on Cooling

As an interstitial diffuser, Fe is relatively mobile even at low temperatures. This mobility provides an opportunity for pairing reactions to occur following the heat treatment. The ionized Fe donor may pair with a stationary acceptor due to the Coulombic interaction between the charged species. At room temperature the following species are in equilibrium

$$Fe_i^+ + B_s^- \leftrightarrow (Fe_iB_s)^\circ \tag{4.12}$$

and the equilibrium constant [33, 34], K, is given by

$$K = [Fe_iB_s]/[Fe_i][B_s] = 10^{-23} \exp(0.65\ eV/kT) \tag{4.13}$$

At room temperature K=8.3 x 10^{-13}. The doping level plays a role in the metal defect configuration by mediation of the pair equilibrium. At room temperature it is assumed that all iron is positively charged and $[Fe^+] + [Fe^+B^-] = [Fe^+]_{tot}$. The concentration of interstitial iron after pairing can be calculated from the following equation

$$[Fe^+] = \frac{-(1+K([B^-]_{tot} - [Fe^+]_{tot})) + \sqrt{(1+K(N_a - [Fe^+]_{tot}))^2 + 4K[Fe^+]_{tot}}}{2K} \quad (4.14)$$

In the above $[B^-]_{tot}$ is given by $[B^-]_{tot} = [B_s\text{-}] + [Fe^+B^-]$. The expression for [FeB] is

$$[FeB] = \frac{(1+K(N_a + [Fe^+]_{tot})) - \sqrt{(1+K(N_a + [Fe^+]_{tot}))^2 - 4K^2 N_a [Fe^+]_{tot}}}{2K} \quad (4.15)$$

Figures 4.3 and 4.4 show the equilibrium defect concentrations of Fe^+ and FeB, respectively, at room temperature following an instantaneous quench from the high temperature indicated.

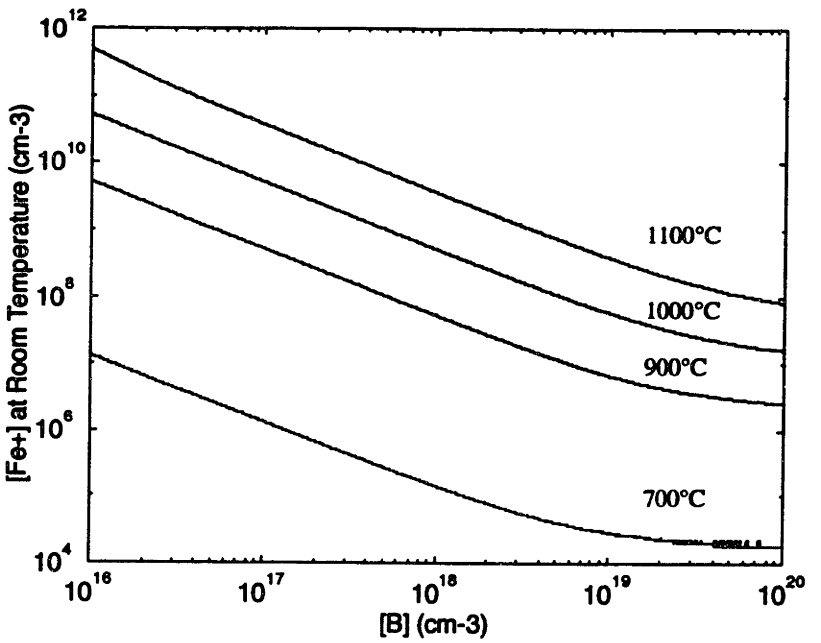

Figure 4.3 Concentration of unpaired Fe^+ as a function of [B] at room temperature following annealing at the temperature indicated and equilibrium pairing reactions.

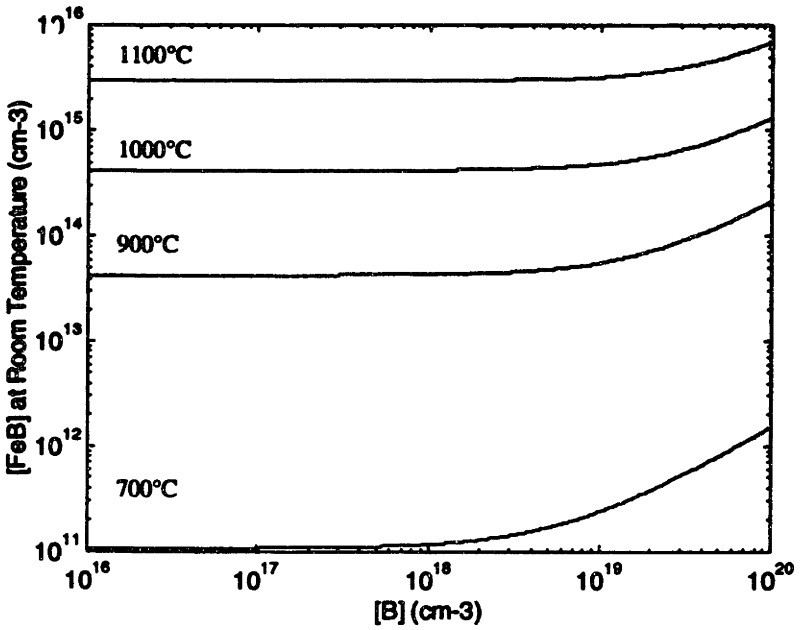

Figure 4.4 Equilibrium concentration of FeB at room temperature as a function of [B] after pairing reactions.

Equilibrium concentrations of the various defect species control the recombination lifetime of the material. The Fe_iB_s complex introduces a shallow level at Ev+0.1eV, distinct from the deep level of the interstitial Fe ion at Ev+0.4eV. [35] The Shockley-Read-Hall (SRH) recombination lifetimes are inversely dependent on defect concentration and capture cross section as given by:

$$\tau_{Fei} = 1/(\sigma_{Fei}\, v_{th}\, [Fe_i]) \tag{4.14}$$

and

$$\tau_{FeiBs} = 1/(\sigma_{FeiBs}\, v_{th}\, [Fe_iB_s]) \tag{4.15}$$

where the values for the capture cross sections have been determined by Zoth and Bergholtz as $\sigma_{Fei} = 5.5 \times 10^{-14}$ cm^2 and $\sigma_{FeiBs} = 5 \times 10^{-15}$ cm^2. [36] The bulk lifetime is given by:

$$1/\tau_{bulk} = 1/\tau_{Fe} + 1/\tau_{FeB} + 1/\tau_{Auger} \tag{4.16}$$

where τ_{Fe} and τ_{FeB} are the SRH recombination lifetimes for Fe and FeB, respectively. Auger recombination, important at high doping levels, is signified by τ_{Auger} and is given by

$$\tau_{Auger} = 1/C\, p_o^2 \tag{4.17}$$

under low injection conditions in a p-type semiconductor. The Auger recombination coefficient, C, in Si is approximately 10^{-31} cm^6/s and p_o is the carrier density.

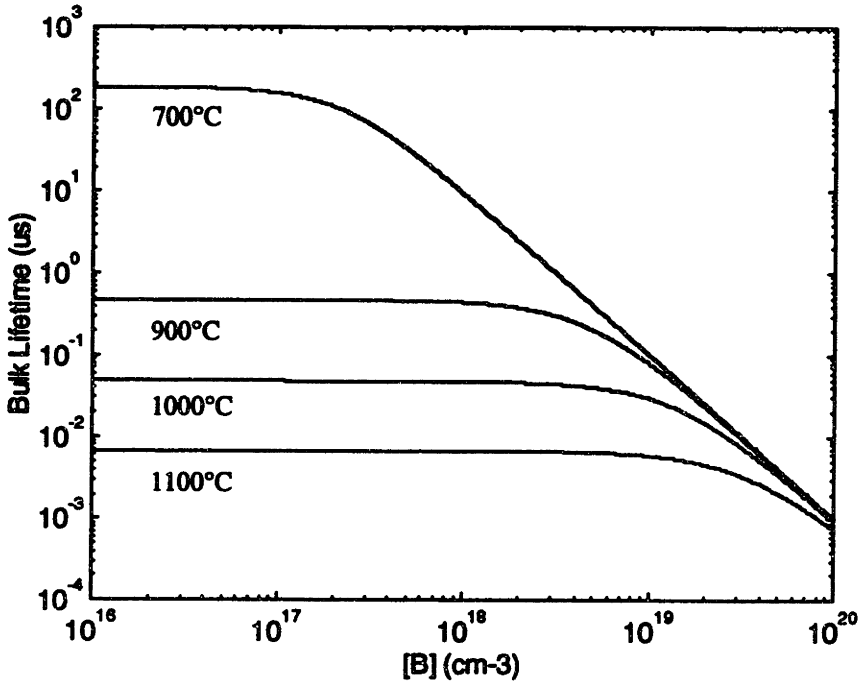

Figure 4.5 Minority carrier lifetime as a function of dopant concentration given the calculated values of defect concentration.

From the results shown in Figure 4.5, we see how high concentrations of Fe can have a detrimental effect on device performance. It has been demonstrated how contamination can be controlled by limiting the temperatures at which processing takes place and by limiting acceptor concentration.

4.4 Segregation to Highly Doped Regions

The modeling of solubility as a function of dopant concentration allows the prediction of the ability of a heavily doped region to getter metallic impurities. The segregation coefficient is defined here as the total solubility in the bulk to the total solubility in the gettering region. Figure 4.6 is a graph that represents the segregation coefficient for Fe at various B concentrations and heat treatment temperatures. The calculations assume that the base concentration is the undoped solubility value [Fe]°.

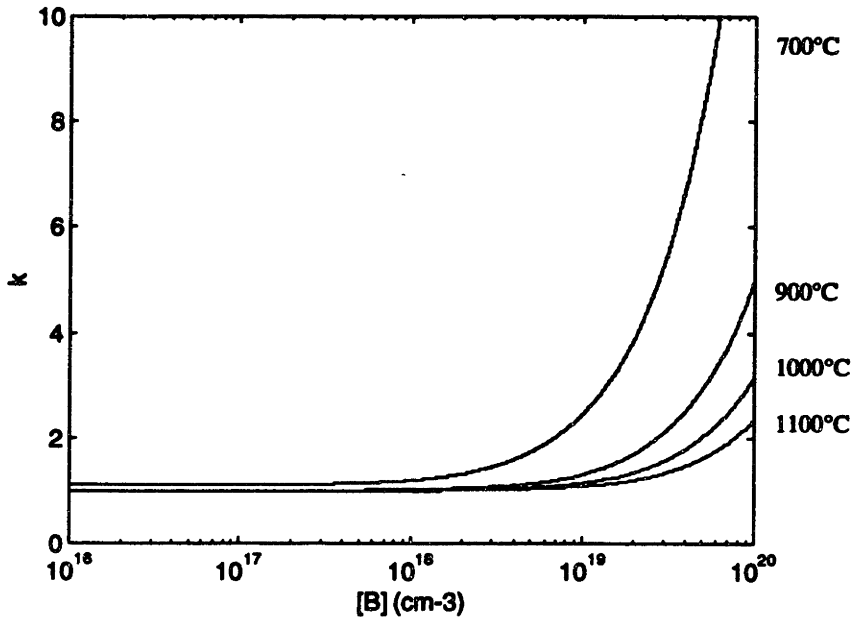

Figure 4.6 Segregation coefficient, k, for iron between a low-doped p region and a p+ layer of the indicated doping concentration at the given temperatures

These segregation coefficients are quite small for doping below 10^{19} cm^{-3} indicating that chemical segregation to the p+ region alone is not responsible for gettering behavior in silicon solar cells. While the segregation coefficient is greater at lower temperatures, total solubility is smaller; therefore, gettering temperature should be chosen with some knowledge of the total contamination of the wafer. When the metal concentration is low, lower gettering temperatures should be used to get the maximum benefit of segregation to the p+ region. If more metal is present, higher temperatures are necessary to dissolve metal precipitates. Figure 4.7 gives the segregation coefficient as a function of temperature, assuming a base doping of 10^{13} cm^{-3} and doping in the p+ layer of 10^{19} cm^{-3}. Because k increases as temperature decreases, control of cooling rates is expected to be important to the effectiveness of segregation gettering.

With the appropriate choice of dopant concentration in base and gettering regions, coupled with an appropriate annealing temperature, control over metallic redistribution can be achieved. Note that the calculations for segregation coefficient do not depend on dopant species, but rather on dopant type (n or p) and concentration. The solubilities of

different dopants determine the maximum achievable segregation coefficient. Equilibrium pairing reactions at room temperature and parameters affected by pairing do depend on dopant species.

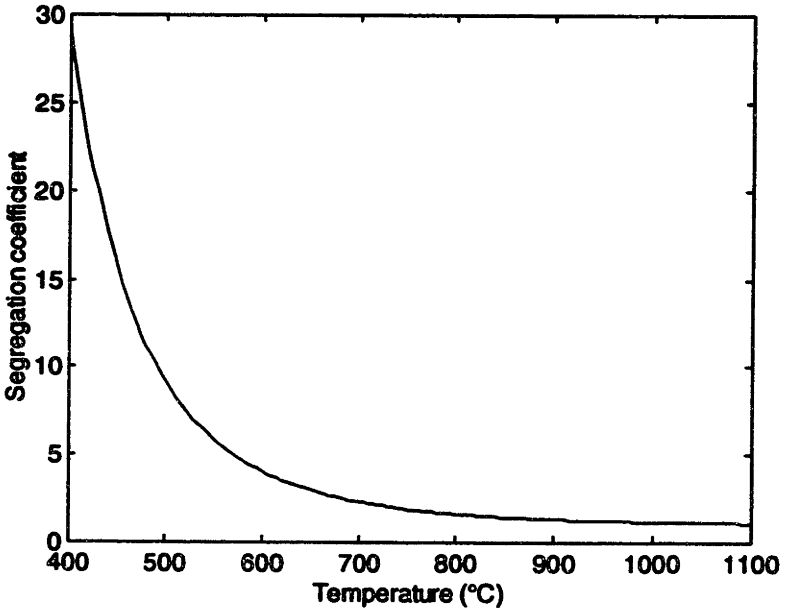

Figure 4.7 Segregation coefficient versus temperature for Fe in B-doped Si. The base doping is 10^{13} cm^{-3} and the doping of the p+ region is 10^{19} cm^{-3}.

4.5 Implications for Processing

Iron contamination is seen to depend strongly on processing temperatures and dopant concentration. This model demonstrates that control over metal contamination is possible by attention to these parameters. We have calculated how pairing reactions at low temperatures influence the recombination lifetime in the material, and thus how cell performance may be affected by certain processing schemes. It is also worthwhile to note that transition metals may be gettered to regions of higher acceptor concentration. Special attention should be paid to cooling rates for maximum benefit of segregation to highly doped regions.

Chapter 5

Modeling Outdiffusion and Precipitate Formation

How metals in silicon behave upon cooling from high temperature processing steps is of interest in all aspects of device fabrication. Solubilities are reduced as temperature drops and the supersaturation of metal atoms creates a driving force for outdiffusion and precipitation. In this chapter we are concerned with the theoretical prediction of haze formation. Haze, the near surface precipitation of metals, occurs as a result of outdiffusion. The occurrence of such outdiffusion is of interest with relation to the ability to getter at surfaces.

5.1 Experimental Background for Haze Formation

Haze is defined as the near surface precipitation of metallic impurities during a moderately fast cooling from high temperature. Outdiffusion is a way of overcoming supersaturation at high temperatures for fast diffusing impurities. As a result, metal concentrations are high near surfaces and precipitation occurs there. Precipitates near the surface of a wafer can be revealed by chemical etching. It is the collective appearance of the etch pits that results in the term haze. A thorough discussion of haze is included in a review by Graff. [24]

A haze test can be performed to detect the presence of nickel and copper, two common wafer contaminants. It consists of a heat treatment at high temperature for a short time, for example, 1050°C for 7 minutes in the case of 10 cm wafers of standard thickness, in an inert atmosphere. The time chosen allows for impurity diffusion throughout the thickness of the wafer. To compare haze test results a standard cooling rate is chosen, usually 4 degrees per second.

Copper, cobalt, nickel, rhodium and palladium are haze forming impurities. Iron will form haze only during subsequent low temperature anneals, although it does enhance precipitation when other haze forming metals are present. No haze is observed in wafers

contaminated with V, Ti, Mn, Cr, Pt or Au. Ranking of haze forming tendency is performed experimentally by using a standard set of processing conditions. Nickel is first, followed by Pd, Co and Cu. Iron forms haze precipitates when shower cooling rates are used.

Haze forming tendency is related to the relative diffusivity and solubility of the metal in Si. Outdiffusion is affected by cooling rate. Solubility, and its change in temperature, are related to metal supersaturation on cooling as well as the distance that must be traveled by metal impurities to form precipitate nuclei or contribute to their growth.

The precipitates that form are silicides. [37] The metals that form haze are believed to precipitate by a homogeneous mechanism. Iron, because it most readily precipitates in the presence of other impurities, is assumed to precipitate heterogeneously. In Section 5.2.2 we see that this is probably not the case. The orientation, distribution and size of precipitates depends on the relative lattice parameters of silicide and silicon. Silicides of cobalt and nickel have lattice constants close to that of Si so their precipitation results in the least strain energy. Large volume changes associated with the formation of Pd and Cu silicides result in the emission of silicon selfinterstitials, as evidenced by dislocation loops inside the precipitate or punched out into the surrounding lattice.

5.2 Historical Approaches to Modeling Precipitate Formation

Transition metals in silicon have high heats of solution compared to systems usually modeled by nucleation theory. Metal solubility is very small and changes by orders of magnitude over short temperature intervals. As a result, nucleation theory is not the best way to model haze formation. However, we dc look to this classical approach to see what it can reveal about the thermodynamics of silicide nucleation. We then turn to pair formation theory as a way of ranking precipitate formation tendency using thermodynamic variables, finding close agreement with experimental observation.

5.1.1 Nucleation Theory

Nucleation theory classically has attempted to explain the kinetics of the earliest stage of phase transformations. Reviews of the theory are given by Russell and Christian and Allen. [38, 39, 40] As in Figure 5.1, the relationship between time and the number of particles can be represented for a system of fixed size undergoing precipitation from a supersaturated solution.

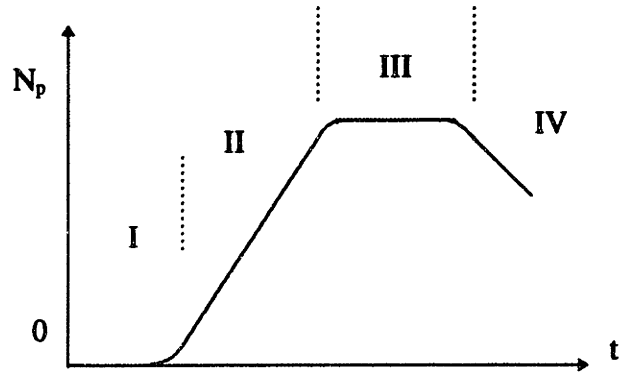

Figure 5.1 Schematic of variation in number of particles versus time during a precipitation reaction

Four regions are illustrated. Region I is the induction period during which the kinetics can be described by:

$$^{v}I(t) = {}^{v}I_s \exp(-\tau/t) \qquad (5.1)$$

where $^{v}I(t)$ is the nucleation rate (number of particles nucleating per unit volume per unit time) and τ is the incubation time. Region II is the steady state nucleation regime. During this time, the nucleation rate is exponentially related to the critical free energy change for nucleation. In region III there is a decreasing rate of nucleation, as would occur as supersaturation decreases. Region IV corresponds to the particle coarsening regime. Here the number of particles decreases as the average particle size increases. For the purposes of this study we only concern ourselves with describing the kinetics of nucleation.

The driving force for precipitation reactions is the reduction in chemical free energy that accompanies the phase transformation. The kinetics of nucleation are largely dependent on interfacial free energies between the parent and product phases. Interfacial energy is in turn dependent on the structure of the interface. Interfacial energy is low for

coherent interfaces (typically 10 to 100 mJ/m^2) and highest for incoherent ones (about 500 mJ/m^2.) The energies play a large role in determining the type of interface present during the nucleation stage since the critical free energy barrier to nucleation, ΔG^*, is proportional to the interphase free energy per unit area, σ, raised to the third power. The value of ΔG^* may be derived from

$$\Delta G = (\Delta g_v + \Delta g_{str})V + \sigma(A) \qquad (5.2)$$

where Δg_v is the chemical free energy change per unit volume transformed, Δg_{str} is the elastic strain energy per unit volume transformed, V is the volume transformed and A is the interphase boundary area.

The nucleation rate I (or J) in the is defined as the number of critical nuclei formed per unit volume per unit time. The steady state nucleation rate is given by:

$$^{v}I_s = K \exp(-\Delta G_c/kT) \qquad (5.3)$$

or

$$J_s = Z \beta^* N \exp(-\Delta G^*/kT) \qquad (5.4)$$

where Z is the Zeldovich non-equilibrium factor, approximately 10^{-2}, β^* is the rate at which atoms are added to the critical nucleus, N is the number of atomic nucleation sites of a particular type per unit volume, and ΔG^* is the free energy change associated with the formation of a critical nucleus.

The critical nucleus has size n* and is given by the point at which the curvature of the plot of ΔG v. n is zero, as illustrated in Figure 5.2.

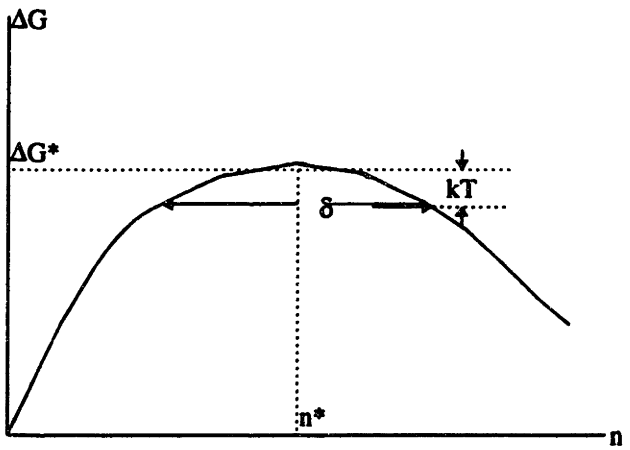

Figure 5.2 Variation in free energy with the size of a precipitate nucleus.

Nuclei of size greater than n* grow while smaller nuclei dissolve. The effect of thermal fluctuations is that microclusters in the size range $n^* \pm \delta/2$, as defined by kT, (see Fig. 5.2) do not have a standard statistical distribution. The net effect is that clusters of size greater than n* do not all continue to grow and reach supercritical size. This effect is accounted for in the Zeldovich factor.

$$Z \approx \delta^{-1} \text{ and } \tau \approx \delta^2/(2\beta^*) = (2Z^2\beta^*)^{-1} \tag{5.5}$$

Russell (1980, p. 249) shows that for homogeneous nucleation in the absence of strain energy effects

$$Z\beta^* \approx D_{eff} X^{\alpha}/a^2 \tag{5.6}$$

where D_{eff} is the effective diffusion constant, X^{α} is the concentration of B atoms present in the matrix (considering a transformation from A-rich phase α to B-rich phase β) and a is the lattice constant.

For an observable rate of homogeneous nucleation of 1 cm^{-3} s^{-1} Δg_v must be less than 70kT.

The alternative to homogeneous nucleation is nucleation at grain boundaries, edges, corners or dislocations. This is termed heterogeneous nucleation. In these cases the energy barrier to nucleation is generally lower due to the reduction of interfacial energy of the critical nucleus. While this is the case, the number of nucleation sites is reduced compared to the homogeneous case. The predominant nucleation mechanism is therefore the one with the faster kinetics.

5.1.2 Modeling Based on Nucleation Theory

In order to determine if nucleation theory could provide a theoretical basis for understanding haze formation behavior, we start with a combination of Equations (5.4) and (5.6).

$$J_s = D_{eff} (X^{\alpha}/a^2) N \exp(-\Delta G^*/kT) \tag{5.7}$$

For these calculations X^{α} is the metal solubility at high temperature, and a is the Si lattice constant. N is the number of nucleation sites. Most metals are assumed to precipitate

homogeneously to form haze. In this case N is 5 x 10^{22} cm^{-3}, the atomic density of silicon. The goal is to compare nucleation rates for various transition metals. We have chosen to compare results for Cu, Ni, Pd, Co, Fe, Cr and Ti. First, we look at the case where a contaminated wafer, with the high temperature maximum concentration of metal, is quenched to a lower temperature.

To approximate ΔG^* we start with Equation (5.2). For nucleation the problem is that of a strained coherent particle because it is assumed that this is the most favorable condition, so σ is taken to be that of a coherent particle (10-100 mJ/m^3) assuming it is the same for all particles. The quantity Δg_{str} can be approximated by relation to the difference in lattice parameters the Si lattice and the metal silicide.

$$\Delta g_{str} = 2\left[\frac{(1+\nu)}{(1-\nu)}\right]\mu(\varepsilon_{11}{}^{T})^2 \tag{5.8}$$

The solubility at different temperatures was used to calculate Δg_v as follows

$$\Delta g_v = kT \ln(\Delta C_s/C_s) \tag{5.9}$$

Expressions used for the solubility and diffusivity of metals are listed in Table 5.1. Lattice constants of the silicides were taken from Murarka. [41]

Table 5.1 Expressions for the solubility and diffusivity of some transition metals

Metal	Solubility (cm^{-3})	Ref.	Diffusivity (cm^2/s)	Ref.
Cu	$5x10^{22}exp(2.4-1.49/kT)$	42	$4.7x10^{-3}exp(-0.43/kT)$	43
Ni	$5x10^{22}exp(3.2-1.68/kT)$	42	$2.0x10^{-3}exp(-0.47/kT)$	43
Pd	$5x10^{22}exp(-0.73-1.61/kT)$	44	$2.6x10^{-3}exp(-0.48$ [illegible]$)$	24
Co	$5x10^{22}exp(7.6-2.83/kT)$	42	$4.2x10^{-3}exp(-0.$ [illegible]$)$	45
Fe	$5x10^{22}exp(8.2-2.94/kT)$	42	$1.3x10^{-3}exp(-0.68/kT)$	42
Cr	$5x10^{22}exp(4.7-2.79/kT)$	42	$1.0x10^{-2}exp(-0.43/kT)$	43
Ti	$5x10^{22}exp(4.22-3.05/kT)$	46	$1.45x10^{-2}exp(-0.43/kT)$	46

When these calculations are carried out, even at small undercoolings, very high nucleation rates result. In the case where the sample was quenched 5 degrees from 1050°C and allowed to relax, the fastest value was 2.6 x 10^{48} $s^{-1}cm^{-3}$ for Ni and the slowest 2.9 x 10^{39} $s^{-1}cm^{-3}$ for Ti. This would indicate that for all metals considered, supersaturation would last for no longer than a second. This trend continues for both

small (5°C) and large (500°C) undercoolings. The nucleation rates calculated are so high because there is no need to wait for diffusion to occur to form a critical nucleus. Values for r*, given by $r^*=-2\sigma/(\Delta g_v + \Delta g_{str})$, are smaller than one angstrom, regardless of the constants chosen for strain energy and surface free energy.

The results are clearly not physically consistent with the definition of precipitate nucleation since the critical nucleus size is smaller than that of even a single atom. ΔG^* is controlled by the chemical free energy change associated with precipitation. We see that the driving force to form precipitates of metals in Si is very large, larger than in classical systems. It is driven by ΔH of the metals. The impurities are only soluble to a small extent, and the solubility changes by orders of magnitude for relatively small changes in temperature. As a result we observe that classical nucleation theory is not useful in predicting haze forming behavior. What is learned is that, based on the energetics of these systems, when two or more metal atoms come together in a supersaturated system, it is highly favorable for them to stay together and form the nucleus of a precipitate. Also, it is seen that for all metals it is thermodynamically favorable to form nuclei by a homogeneous mechanism, regardless of actual haze forming tendency, because the role of surface energy is not significant.

5.3 Pair Formation Theory to Predict Haze

5.3.1 Pair Formation Model

Because it is reasonable to look to pair formation to understand the nucleation of metal silicides in Si, we turn to the Reiss model for pair formation. [47] The expression for the time constant for pair formation is given by

$$\tau = f/4\pi RDN \qquad (5.10)$$

where f is the fraction of atoms paired or precipitated at equilibrium, R is the capture radius, D is the diffusion coefficient and N is the density of sites available for pairing. The rate of pair formation can be expressed as $1/\tau$. The above equation represents the general case, and $1/\tau$ can be thought of as a precipitation rate, the rate at which atoms are leaving

solution. If we assume that each metal atom is a potential nucleation site, then before any pairing takes place N is C_s. If these atoms are equally spaced, then we can take $R=C_s^{-1/3}$. The result is the following relationship.

$$\tau = f/4\pi C_s^{2/3} D \qquad (5.11)$$

The nucleation rate, the initial rate at which precipitates form, is thus proportional to $C_s^{2/3}D$. The value of f can be calculated based on a comparison of high and low temperature solubilities. In this way the model takes into account the parameters expected to most influence haze formation behavior.

5.3.2 Calculations Based on Pair Formation

Two methods were used to do calculations. First, consider a rapid quench from high to low temperature. In this example, high temperature is taken to be 1050°C and the samples are instantaneously quenched to 500°C. If it is assumed that the metal concentration reaches the solubility limit at high temperature, calculations yield the nucleation rates as shown in Table 5.2. If allowances are made for changes in metal concentration as pairing reactions take place, it is found that for short times, on the order of several minutes, pairing rates do not change.

Table 5.2 Rate of removal of metal atoms from supersaturated solution at 500°C after a quench from 1050°C.

Metal	Rate (s^{-1} cm^{-3})
Cu	1.0×10^{8}
Ni	1.3×10^{7}
Pd	1.6×10^{6}
Co	2.6×10^{5}
Fe	6.6×10^{3}
Cr	113
Ti	1.6×10^{-4}

An observable nucleation rate is considered to be greater than 1 s^{-1} cm^{-3}. Since here we are actually not looking at a nucleation rate, but at the rate of pair formation or of addition of atoms to an existing precipitate, we are not seeing a nucleation rate, and can

expect an observable effect for rate values that correspond to the number of atoms in a precipitate. Typical nickel silicide precipitates are spherical with radii from 5 to 25 nm. Iron precipitates are rod-shaped with dimensions on the order of 10x10x100 nm. [24] Thus the typical silicide precipitate contains roughly 10^4 to 10^5 metal atoms per cubic centimeter. This puts the observable dissolution between that for iron and cobalt.

Other calculations involve cooling from high temperature to room temperature at a rate of 4K/s, the standard cooling rate for the haze test. Calculations involved taking small steps in temperature as it related to time, and calculating the pairing rate and number of atoms paired/precipitated during each step. After the first step, and in all subsequent steps, N and R were adjusted by subtracting the number of pairs that had formed from the high temperature solubility value and by letting $R=N^{-1/3}$. Also after the initial step, what is termed pair formation could really indicate the addition of one atom to a precipitate that already existed. These calculations give pairing/growth rates as a function of temperature, and the total number of precipitated atoms after the cooling step. Results are shown in Figure 5.3 showing the predicted ranking of precipitation tendency. This ranking of follows experimental observations for haze formation except in the case of copper. Table 5.3 gives values for the number of precipitated metal atoms after the scheduled cooling. This is compared to the amount precipitated at equilibrium at room temperature. In all cases significant supersaturation of metal remains following this cooling schedule.

Table 5.3 Number of atoms precipitated and the equilibrium number of atoms precipitated for cooling from 1050°C to room temperature at 4°C/s.

Metal	Atoms Precipitated (cm^{-3})	Equilibrium Number Atoms Precipitated at Room Temperature (cm^{-3})
Cu	2.7×10^{11}	1.2×10^{18}
Ni	4.0×10^{10}	4.8×10^{17}
Pd	5.3×10^{9}	1.8×10^{16}
Co	7.6×10^{8}	1.7×10^{15}
Fe	4.4×10^{7}	1.2×10^{15}
Cr	4.7×10^{6}	1.3×10^{14}
Ti	730	8.2×10^{12}

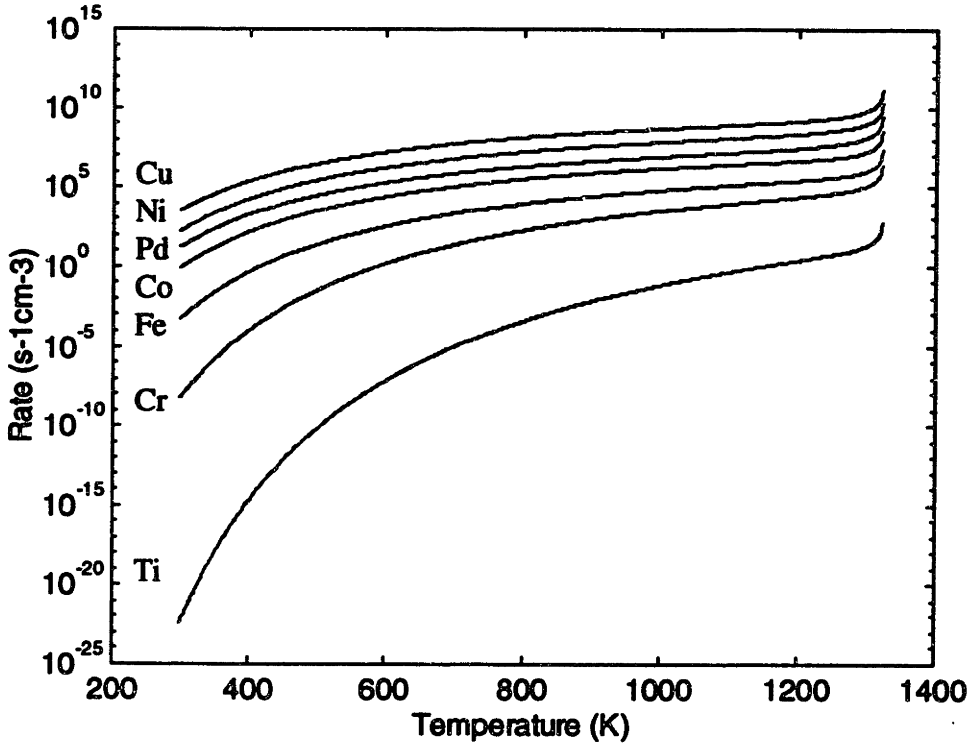

Figure 5.3 Rate of removal of atoms from supersaturated solution on cooling at 4°C/s from an annealing temperature of 1050°C. Pairing rates are strongly dependent on temperature and drop off rapidly.

Note that this calculation does not consider the effects of outdiffusion; however, it is reasonable to assume that outdiffusion would be influenced by metal diffusivity and concentration which have already been considered (in some way) in this model. In the case of outdiffusion, the surface acts as a bias to diffusion direction. The model also does not include stress considerations which become important as the precipitates grow. Because there is a large volume change associated with precipitation, this could explain why the ranking of copper in the model is different from experiment.

5.4 Other Considerations

In gettering studies it is noted that precipitation occurs preferentially at dislocations and other lattice defects. Based on the energetics of nucleation, we see no

reason for this to be the case. However, as a precipitate grows coherency strain and surface energy considerations may influence preferential sites. When large volume changes are associated with precipitation, strain energies and injection of vacancies or selfinterstitials to the lattice may retard precipitate growth. When this is true, the precipitates most likely to grow are those near surfaces or lattice defects where strain energy may be compensated, surface energy change for the system upon precipitation is reduced, or where there is a source or sink for intrinsic defects.

The precipitation of Fe is enhanced in samples also contaminated with Cu. Defect equilibrium and strain energy effects can possibly explain this. For each copper atom precipitated approximately 0.55 silicon interstitials are emitted. The precipitation of Fe results in the absorption of 0.11 silicon atoms per metal atom. The energetics of strain and Si interstitial supersaturation may be such that coprecipitation is favored.

At low temperature, when stress from the aluminum film is present, precipitation and outdiffusion could be influenced. Precipitation at the rear of the cell which is under compression becomes more favorable for iron silicide which has a negative change of volume on formation, and less favorable for the other haze forming metals whose silicides are larger than the silicon lattice. The effect should be strongest for Cu and Pd. This is mainly an issue at low temperature where diffusion limited precipitation occurs slowly.

Chapter 6

Effect of Alloying on Carrier Lifetime

The gettering mechanisms discussed in Chapters 3, 4 and 5 combined with the lowering of the effective surface recombination velocity contribute to the increase in minority carrier lifetime following the alloying step. Radio Frequency Photoconductance Decay (RFPCD) was used to monitor lifetime improvements associated with this processing step. It was found that lifetime improves with annealing time at a given processing temperature. Higher processing temperature results in a faster increase in carrier lifetime.

6.1 Measurement Procedure

RFPCD uses a pulsed light source to excite excess minority carriers and RF power to monitor carrier decay. This is a contactless measurement system, capable of probing bulk recombination lifetimes for carrier densities of greater than 10^{19} cm^{-3} for a 500 μm thick wafer.

Measurements were carried out with the wafer immersed in an HF (48%) bath to provide for surface passivation. All wafers were cleaned before measurement. After the initial measurement on a clean p-type wafer, Al was deposited on both sides by e-beam evaporation. The desired furnace anneal followed. The resulting structure consists of a p+ layer on both sides of the wafer, capped by the Al with Si in the eutectic structure. The metal was stripped in a concentrated HCl solution and the wafer was cleaned prior to the post-anneal lifetime measurements.

6.2 Effect of Time and Temperature on Lifetime

Lifetime measurements were taken before and after deposition of 2 micron thick layers of Al on both sides of p-type wafers. First, the effect of varying process time is considered. The alloying temperature was 850°C and annealing times varied from 3 minutes to one hour. There was considerable scatter in the results so we show the maximum values for lifetimes corresponding to the alloying times in Figure 6.1. Lifetimes higher than original values indicate gettering as well as the effectiveness of the p+ layer in reducing the effect of surface recombination. Note that longer alloying times show an increase in measured lifetime, but with decreasing benefit as time progresses. The degree of scatter in the post-annealing lifetimes reflects the degree of roughness of the p-p+ interface and the back surface.

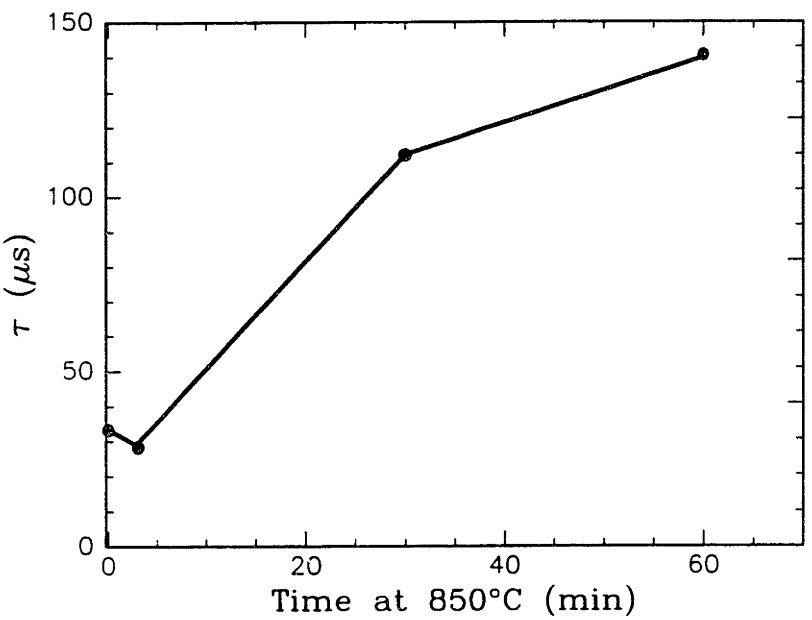

Figure 6.1 Best value of bulk minority carrier lifetime versus annealing time at 850°C.

By annealing at higher temperatures, the improvement in lifetime occurs more quickly. Figure 6.2 shows average measured lifetimes for wafers annealed for three minutes at 850°C, 950°C and 1050°C. These wafers had all been deposited with 2

microns of Al on both sides and annealed in a nitrogen ambient. Faster diffusion and higher solubility at 1050°C cause significant gettering to occur in the short annealing time.

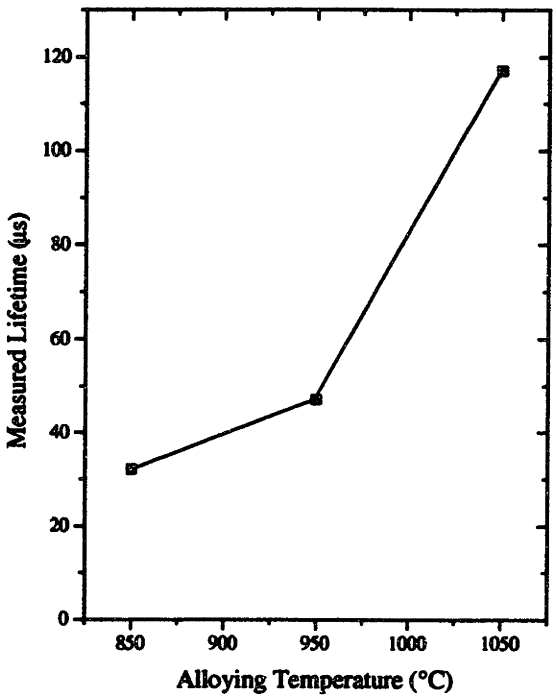

Figure 6.2 Average bulk minority carrier lifetime versus processing temperature for 3 minute annealing times

Surface roughening is severe, but the recrystallized p+ layer effectively compensates for this. Smoother surfaces, such as those achieved by rapid thermal annealing, are expected to result in even greater measured lifetime values.

These results show that gettering of contaminants from these wafers is improved by longer times at high temperature or by higher temperatures. This is expected, given that adequate time must be allowed for defect species to diffuse to the contact region. Higher temperatures may be required for very contaminated material, so that precipitates can be fully dissolved. As time progresses, the advantage of continued annealing is reduced. A balance must be struck between improved performance and processing time and cost.

Chapter 7

Solar Cell Process Design

The goal of the work done to understand gettering behavior and details of alloyed backside contact formation is to provide insight into how to better manufacture solar cells. A summary of the results leads to conclusions about what should be effective in improving solar cell processing. It is suggested that further work be done to verify the ideas put forth here.

7.1 Application to Back Surface Field

This work demonstrates several ways the processing of solar cells can be performed to improve the performance of the back surface field. These relate to interface morphology, doping of the recrystallized layer and stress due to the Al contact.

The smoothest interfaces observed for alloyed contacts result from rapid thermal annealing. These are therefore the best choice for producing contacts. High temperature RTA followed by remelting in a at lower temperatures may be useful for control of other desirable effects, such as gettering, without compromising the uniformity of the junction. Because it has been observed that junction depth is much greater than expected based on the phase diagram, it is suggested that testing by EBIC be done to verify the distance of the p-p+ junction from the Al contact.

Nonequilibrium effects are observed with relation to doping of the recrystallized Si, even with moderately slow cooling. This is advantageous because it allows higher Al concentrations in Si and provides for a more uniformly doped p+ region. It should be verified that Al precipitates do not form upon cooling, especially if subsequent processing steps are carried out at elevated temperature, as this would result in poorer cell performance.

Slow cooling rates would help to minimize stress because relaxation occurs faster at elevated temperature. An effective way to reduce stress is to use higher temperatures

for the alloying step. This would allow the use of less Al for the same desired p-p+ junction depth.

7.2 Application to Gettering

The modeling of segregation coefficient and haze formation suggests applications for processing related to gettering. With respect to segregation gettering, we see that higher doping or lower temperature has the potential for more effect. High doping is compatible with cell processing because of the associated advantage of reducing S_{eff}. This suggests high alloying temperatures. Slow cooling rates, or cooling and holding at moderate temperature could improve gettering by taking advantage of high segregation coefficients.

The results related to haze formation suggest some things about outdiffusion and precipitate formation of transition metals. We find that solubility (as well as changes in solubility) and diffusivity are key factors in understanding the causes of haze formation. Calculations based on classical nucleation theory predict that iron does not require heterogeneous nucleation sites as has been assumed. Instead, we see that for Fe the kinetics of nucleation are slower. This is responsible for behavior.

The difference in theoretical and experimental rankings of Cu precipitation and growth may be due to stress related issues. While precipitation is energetically favorable, growth may be hindered by strain energy associated with lattice mismatch. Nickel silicide and cobalt silicide have small lattice mismatch with silicon, making it much easier for these precipitates to form and grow. Calculations of interfacial strain energy associated with silicide precipitates, or energies associated with forming dislocations to relieve strain, could provide insight into this issue.

Cooling rates, especially at high temperature, will determine to what degree outdiffusion and precipitation will occur. The highest precipitation rates are expected at high temperature, and drop off rapidly (as does D) with cooling.

7.3 Conclusions

Because cooling rate and treatment temperature are important special attention should be paid to cooling of the sample after the alloying step, as well as the parameters of any subsequent processing steps. These factors are as likely to influence device performance as the time and temperature of the alloying step itself. In general the recommendations are for rapid heating to a high alloying temperature and slow cooling, possibly coupled with subsequent anneal at a lower temperature.

Bibliography

1. R. H. Bube, "Materials for photovoltaics," *Annu. Rev. Mater. Sci.*, **20** (1990), pp. 19-50.
2. A. Rohatgi, E. R. Weber and L. C. Kimerling, "Opportunities in silicon photovoltaics and defect control in photovoltaic material," *Journal of Electronic Materials*, **22**, 8 (1993), pp. 65-72.
3. R. Gereth, H. Fischer, E. Link, S. Mattes and W. Pschunder, "Contribution to the solar cell technology," *Energy Conversion*, **12** (1972), pp. 103-107.
4. J. Mandelkorn, C. McAfee, J. Kesperis, L. Schwartz and W. Pharo, "Fabrication and characteristics of phosphorous-diffused silicon solar cells," *J. Electrochem. Soc.* (1962) pp. 313-318.
5. P. A. Iles, "Increased output from silicon solar cells," *8th IEEE Photovoltaic Specialists Conf.*, Seattle (1970), pp. 345-352.
6. M. P. Godlewski, C. R. Baraona, H. W. Brandhorst, Jr., "Low-high junction theory applied to solar cells," *10th IEEE Photovoltaic Specialists Conf.*, Palo Alto, California (1973), pp. 40-47.
7. J. Mandelkorn and J. H. Lamneck, Jr., "Simplified fabrication of back surface electric field silicon cells and novel characteristics of such cells," *9th IEEE Photovoltaic Specialists Conf.*, Silver Spring, Maryland (1972), pp. 66-71.
8. J. Mandelkorn and J. H. Lamneck, Jr., "A new electric field effect in silicon solar cells," *J. Appl. Phys.*, **44**, 10 (1973), pp. 4785-4787.
9. M. A. Green, "Silicon solar cells: evolution, high efficiency design and efficiency enhancements," *Semicond. Sci. Technol.*, **8** (1993), pp. 1-12.
10. R. R. King, E. W. Thomas, W. B. Carter and A. Rohatgi, "The effect of aluminum and boron solid-source doping on recombination in silicon solar cells," *22nd IEEE Photovoltaic Specialists Conf.* (1991), pp. 229-234.
11. J. del Alamo, J. Eguren and A. Luque, "Operating limits of Al-alloyed high-low junctions for BSF solar cells," *Solid State Electronics*, **24** (1981), pp. 415-420.
12. B. Hartiti, J. C. Muller, A. Slaoui, P. Siffert and D. Sarti, "Back surface field-induced gettering in multicrystalline silicon," *22nd IEEE Photovoltaic Specialists Conf.* (1991), pp. 998-1001.
13. J. H. Wohlgemuth and S. Narayanan, **Photovoltaic Concentrator Initiative Concentrator Cell Development** (Contract Report), SOLAREX Corp., Frederick, Maryland (1993).
14. P. Lölgen, "Surface and volume recombination in silicon solar cells," Ph. D. Thesis, CIP-Gegevens Koninkluke Bibliotheek, Den Haag (1995).
15. M. A. Green, **Solar Cells: Operating Principles, Technology and System Applications**, University of New South Wales, Kensington, Australia (1992).
16. M. A. Green, **Silicon Solar Cells: Advanced Principles and Practice**, University of New South Wales, Kensington, Australia (1995).

17. C. Hu and R. M. White, **Solar Cells: From Basics to Advanced Systems**, McGraw-Hill Book Company, New York (1983).
18. T. B. Massalski, J. L. Murray, L. H. Bennett and H. Baker, eds., **Binary Alloy Phase Diagrams**, Volume 1, American Society of Metals, Metals Park, Ohio, p. 165.
19. O. Madelung and M. Schultz, eds, **Semiconductors: Impurities and Defects in Group IV Elements and III-V Compounds**, Vol. III/22b, Landolt-Bornstein, New York (1989).
20. I. Blech, "Stresses in thin film used in microelectronic devices," publication from manufacturer of Tencor stress measurement system.
21. Claeys and J. Vanhellemont, "Recent progress in the understanding of crystallographic defects in silicon," *Journal of Crystal Growth*, **126** (1993), pp. 41-62.
22. J. Lindmayer, *Method for the Post Alloy Diffusion of Impurities into a Semiconductor*, U. S. Patent 3,895,975 (1975).
23. M. Joshi, U. M. Gosele, and T. Y. Tan, *J. Appl. Phys.* **77**, 8 (1995), pp. 3858-3863.
24. K. Graff, **Metal Impurities in Silicon--Device Fabrication**, Springer Series in Materials Science 24, ed. by Hans-Joachim Queisser, Springer-Verlag, New York (1995).
25. J. S. Kang and D. K. Schroder, "Gettering in silicon," J. Appl. Phys., 65 (1989), pp. 2974-2985.
26. R. D. Thompson and K. N. Tu, *Appl. Phys. Lett.*, **41** (1982), p. 440.
27. P. Sana, A Rohatgi, J. P. Kalejs and R. O. Bell, *Appl. Phys. Lett.*, **64** (1994), p. 97.
28. M. Apel, I. Hanke, R. Schindler and W. Schroter, "Aluminum gettering of cobalt in silicon," *J. Appl. Phys.*, **76**, 7 (1994), pp. 4432-4433.
29. H. M'saad, "The role of surface and bulk perfection in the processing and performance of crystalline silicon," Ph. D. Thesis, Massachusetts Institute of Technology (1994).
30. H. Conzelman, K. Graff and E. R. Weber, *Appl. Phys. A*, **30** (1983), p. 169.
31. M. Hourai, K. Murakami, T. Shigematsu, N. Fujino and T. Shiraiwa. *Jpn. J. Appl. Phys*, **28** (1989), p. 2413.
32. H. Reiss, C. S. Fuller and F. J. Morin, "Chemical interactions among defects in germanium and silicon," *Bell Syst. Tech. J.*, **35** (1956) p. 535. Also, H. Reiss and C. S. Fuller, *J. Metals*, **12** (1956), p. 276.
33. L. C. Kimerling, J. L. Benton and J. J. Rubin, "Transition metal impurities in silicon," in **Defects and Radiation Effects in Semiconductors** 1980, Inst. Phys. Conf. Ser. No. 59 (1980), p. 217.
34. L. C. Kimerling and J. R. Patel, in **VLSI Electronics: Microstructure Science 12**, ed. by N. G. Einspruch and H. Huff, Academic Press (1985), p. 223.
35. K. Graff and H. Pieper, *J. Electrochem. Soc.*, **128** (1991), p. 669.
36. G. Zoth and W. Bergholz, *J. Appl. Phys.*, **67** (1990), p. 6764.
37. K. Graff, "Characterization of haze-forming precipitates in Si," *J. Appl. Phys.* **63** (1988), pp. 4444-4450.
38. K. C. Russell, "Nucleation in solids: the induction and steady state effects," *Adv. Colloid Int. Sci.*, **13** (1980), pp. 205-318.

39. J. W. Christian, **Theory of Phase Transformations in Metals and Alloys, Part I,** Pergamon, Oxford (1975).
40. S. M. Allen, **Fundamentals of Solid-Solid Phase Transformations,** (3.31 Lecture Notes) Massachusetts Institute of Technology, Cambridge, Massachusetts (1992).
41. S. P. Murarka, **Silicides for VLSI Applications,** Academic Press, New York (1983).
42. E. R. Weber, *Appl. Phys. A*, **30** (1983), p. 1.
43. K. Graff, in **Semiconductor Silicon 1986,** ed. by H. R. Tuff, T. Abe and B. Kolbesen, Electrochemical Society, Pennington, New Jersey (1986).
44. K. Graff, H. A. Hefner and H. Pieper, *MRS Proc.*, **36** (1985), p. 19.
45. D. Giles, W. Schroter and W. Bergholtz: *Phys. Rev. B*, **41** (1990), p. 5770.
46. S. Hocine and D. Mathiot, **Materials Science Forum,** Vols. 38-41, ed. by G. Ferenczi, Trans. Tech. Aedermannsdorf, Switzerland (1989), p. 725.
47. H. Reiss, *J. Chem. Phys.*, **25**, 3 (1956), pp. 400-413.

THESIS PROCESSING SLIP

FIXED FIELD: ill _____ name _____

index _____ biblio _____

▶ COPIES: (Archives) Aero Dewey Eng Hum

Lindgren Music Rotch (Science)

TITLE VARIES: ▶☐ _____

NAME VARIES: ▶☐ _____

IMPRINT: (COPYRIGHT) _____

▶ COLLATION: 61ℓ

▶ ADD. DEGREE: _____ ▶ DEPT.: _____

SUPERVISORS: _____

NOTES:

cat'r: date:

page: J107

▶ DEPT: Mat Sci & E

▶ YEAR: 1996 ▶ DEGREE: M.S.

▶ NAME: CHALFOUN, Lynn Louise